Spray-made porous CuO-CeO_2 microspheres rival precious metal catalysts for the low-temperature oxidation of air pollutants

*G. Pampararo[a ‡], E. Sartoretti[b ‡] *, A. S. Traoré[c], O. Ersen[c], C. Novara[b], S. Bensaid[b], D.P. Debecker[a] **

[a] Université catholique de Louvain (UCLouvain), Institute of Condensed Matter and Nanosciences (IMCN), Place Louis Pasteur, 1, 1348 Louvain-la-Neuve, Belgium
[b] Department of Applied Science and Technology (DISAT), Politecnico di Torino, Corso Duca degli Abruzzi 24, 10129, Torino, Italy
[c] Institut de Physique et de Chimie des Matériaux de Strasbourg (IPCMS), UMR 7504, Université de Strasbourg-CNRS, 23, Rue du Loess, 67200 Strasbourg, France

*enrico.sartoretti@polito.it
*damien.debecker@uclouvain.be

‡ G. Pampararo and E. Sartoretti contributed equally to this work as first authors

KEY WORDS: Aerosol-Assisted Sol-Gel, Copper-ceria catalysts, Redox catalysis, CO oxidation, VOC total oxidation.

ABSTRACT
Environmental constraints regarding the abatement of toxic gaseous pollutants such as carbon monoxide and various volatile organic compounds (VOCs) demand catalysts that can completely oxidize these molecules at low temperature. There is, however, a growing reluctance towards utilizing catalysts based on expensive and depleting precious metals such as Rh, Pd, and Pt. In this work, a continuous, one-step, and scalable procedure for the synthesis of high-performance copper-ceria catalysts is proposed. The aerosol-assisted sol-gel technique (AASG) allowed preparing porous $CuO\text{-}CeO_2$ catalysts with high specific surface area (up to 140 m^2/g), highly dispersed copper oxide nanoparticles (3-5 nm) in close interaction with ceria crystallites (5-8 nm), high concentration of defects, and abundant reactive oxygen species. This resulted in unprecedented total oxidation activity levels for Cu-Ce-based catalysts. The best catalyst is almost on par with a state-of-the-art oxidation catalyst (based on Pd and Rh) in the total oxidation of ethylene. For CO oxidation, all the synthesized $CuO\text{-}CeO_2$ catalysts reached 90% of conversion at about 85 °C, clearly outperforming the benchmark catalysts by 20-30 °C. The structural properties and superior performances of these new nanostructured copper-ceria catalysts were stable over a 30-hour period, without observable deactivation.

1. INTRODUCTION

The catalytic abatement of environmental pollutants is a continuous challenge for both academic community and various industrial sectors. Among the most significant sources of pollution, emissions derived from vehicles must certainly be accounted for. Exhaust gas from automotive engines contains volatile organic compounds (VOCs), carbon monoxide (CO), particulate matter (PM), and nitrogen oxides (NO_x), most of which need to be converted to CO_2, steam, and nitrogen (N_2) by catalytic converters. [1] Among these substances, VOCs and CO are known to critically affect the air quality in densely populated regions.

The most commonly employed commercial catalytic systems for the abatement of pollutants in the automotive sector are the so-called Three-Way Catalyst (TWC) and Diesel Oxidation Catalyst (DOC). [2–4] These technologies, developed after the 1970s, allow the efficient and simultaneous oxidation of unburnt hydrocarbons and CO, coupled with NO_x reduction in TWC.[5] Typically, these systems consist of a ceramic monolith containing noble metals (usually Pd, Pt and Rh in variable amounts), a redox oxide (such as CeO_2), a high surface area carrier, and possibly some promoters. Their high efficiency is based on the synergy between the different active species [6], and even with low metal loadings (often between 0.5 and 1 wt%) high catalytic activity can be achieved. Catalysts containing other noble metals, such as Ir [7,8] or Au [9,10], have also been explored for the abatement of the pollutants formed in combustion engines. Nevertheless, the use of rare, depleting, and expensive metals generates many concerns about long-term applications, supply, and sustainability.

In this context, alternatives have been explored. [11] With the idea to develop noble metal-free catalysts, many active components and promoters have been investigated such as TiO_2, Fe_2O_3, SnO_2, Co_3O_4, MnO_x, Al_2O_3 and CeO_2, in particular for CO and VOCs oxidation. [12] Among these, CeO_2 has gained interest [13,14] because of its large oxygen storage (and release) capacity (OSC) due to its peculiar redox properties. Indeed, a material with a high OSC helps maintaining stoichiometric composition of gases during air-to-fuel oscillations, by releasing and storing oxygen under fuel-lean and fuel-rich conditions, respectively. [15] Ceria-based catalysts have also been studied in combination with other rare earths such as La, Nd, Pr [16,17], or with transition metals such as Ag [18], Au [19], or Cu. [20–23]

Ceria-supported Ag and Au catalysts have been demonstrated to have superior activity [24–26], but their application is still hindered by their relatively high cost and limited stability. [27] At the same time, copper-ceria catalysts have also exhibited similar performance, attributed to a synergy between ceria and copper oxide. The interactions of two redox couples (Ce^{3+}/Ce^{4+} and

Cu^{1+}/Cu^{2+}), the formation of more oxygen vacancies, and the higher reducibility of the mixed oxide compared to the individual ones, are some of the crucial characteristics responsible for the high activity of these catalysts. [22] Intimacy between copper and cerium species is one of the key parameters to achieve good performance. Following this direction, various advanced synthesis techniques have been explored to prepare highly active CuO-CeO_2 systems, even achieving full CO conversion in the 110-120 °C temperature range. [28–31] Nevertheless, many of these catalyst preparation procedures are time- and energy-consuming, multi-step, and are not directly suitable for scale up processes.

Techniques based on spray drying offer a powerful alternative for the preparation of functional materials. [32] Recent reports have presented ceria-based catalysts made by spray pyrolysis, based on the high-temperature decomposition of Ce precursors in a flame, and yielding non-porous CeO_2 nanoparticles. [33–35] Alternatively, the "aerosol-assisted sol-gel" process (AASG) has demonstrated tremendous potential for the preparation of porous composites. [36] This method is based on a low-cost, continuous, scalable, and environmentally benign sol-gel chemistry process, often coupled with the evaporation-induced self-assembly (EISA) concept. It allows producing micrometric or submicrometric inorganic or hybrid organic–inorganic particles, featuring tunable and calibrated porous structures at different scales, including porous ceria-based materials. [37,38]

In this work, reasoning that the AASG method is primed to promote CuO dispersion and intimate interaction with CeO_2, we exploited it to prepare a new type of highly active oxidation catalysts. Copper was directly introduced in various amounts during the synthesis of porous ceria microspheres. For comparison, pristine ceria microspheres were also prepared and then loaded with CuO via incipient wetness impregnation (IWI). The physico-chemical and morphological properties of all the catalysts were comprehensively investigated, and their performance (activity and stability) was assessed in the total oxidation of CO and ethylene. These novel materials were shown to compete with or even outperform state-of-the-art and commercially available benchmark catalysts.

2. EXPERIMENTAL

2.1. Catalysts preparation

2.1.1. *One-pot preparation of CuO-CeO_2 by aerosol-assisted sol-gel (AASG)*

Solution A [40 g of ethanol (VWR, >99.8%), 4 g of distilled water, 0.4 g Pluronic F127 (Sigma Aldrich)] and solution B [40 g of ethanol (VWR, >99.8%), 4 g of distilled water, 1.5 g of $Ce(NO_3)$•$6H_2O$] were prepared and stirred overnight, then mixed together. Cu nitrate [$Cu(NO_3)_2$•$2.5H_2O$ (Alfa Aesar, 98%)] was added to the resulting solution to reach a copper loading of 5, 10, or 20 wt%. The final solution was then sprayed with an atomizer from TSI© with an air pressure of 30 psi. The aerosol was processed by passing through a quartz tube heated at 450 °C. The dried powder was collected on a nitrocellulose filter (Sartorius Stedim, 0.45 μm). Powders were calcined in a muffle furnace under static air, first at 350 °C (1 °C min^{-1}) for 2 h, and then at 450 °C (1 °C min^{-1}) for 1 h. These catalysts were denoted as "A-Cux-Ce" where x is the Cu wt% that has been calculated as follow: $x = 100*m_{Cu}/(m_{CeO2}+ m_{Cu})$. A pristine ceria catalyst was also prepared following the same protocol, but omitting the addition of copper nitrate; this sample was labelled CeO_2.

2.1.2. *Cu impregnation on preformed CeO_2*

Copper was loaded onto CeO_2 through an incipient wetness impregnation (IWI) protocol, using $Cu(NO_3)_2$*$2.5H_2O$ (Alfa Aesar, 98%) as precursor. The amount of impregnation solution (and its concentration) was calculated starting from the measured pore volume. The copper solution was added to the support, drop by drop with a syringe, to obtain a homogeneous dry dough. The catalysts were then dried at 110 °C (1 °C min^{-1}) for 2 h and further calcined at 450 °C for 1 h (2 °C min^{-1}). The impregnated catalysts were denoted as "I-CuxCe" where x is the Cu wt%.

2.1.3. *Benchmark catalysts*

For comparison, three different benchmark catalysts were considered in this work:

i) "I-Cu10Ce-comm" was prepared by IWI of $Cu(NO_3)_2$*$2.5H_2O$ (Alfa Aesar, 98%) over commercial cerium oxide nanoparticles (CeO_2-Sigma Np, particle size <25 nm, Sigma-Aldrich, 99.95%) to achieve a nominal Cu loading of 10 wt%.

ii) "Cu10Ce-vortex" was prepared in a multi-inlet vortex reactor, according to a procedure reported in reference [31]. Briefly, four syringes were connected to the reactor inlets: two of them were filled with 60 mL of a 0.1 M solution of NaOH (Merck, 98%), while the other two contained 60 mL of a 0.1 M solution of $Ce(NO_3)_3$*$6H_2O$ (Merck, 99%) and $Cu(NO_3)_2$*$3H_2O$ (Merck, 99.5%), in the required amounts to obtain a 10 at% Cu content in the final catalyst. A KD Scientific KDS220 infusion syringe pump (USA) was used to inject the solutions in the vortex reaction chamber, with a 20 mL min^{-1} flow rate. The suspension obtained at the reactor

outlet was stirred at room temperature (RT) for 1 h, centrifuged, and washed multiple times with ultrapure Milli-Q water. The powder was finally dried at 60 °C for 16 h and calcined in static air at 650 °C for 4 h.

iii) "TWC" consists in a noble metal-based formulation developed by one of the world's leading catalyst manufacturers such as BASF, Johnson Mattey, Umicore. This material is used in commercial TWC monoliths, with the aim of abating CO and unburned hydrocarbons produced in spark-ignited internal combustion engines. The powder was gently scraped from the channel walls of an inner section of a monolith. This catalyst contains approximately 0.9 wt% of Pd and 0.1 wt% of Rh, supported on a mixed oxide mainly consisting of Al_2O_3, CeO_2 and ZrO_2.

2.2. Catalysts characterization

The copper loading was assessed through inductively coupled plasma-mass spectrometry (ICP-MS), using a Thermo Scientific iCAP RQ ICP-MS instrument (USA). Prior to the measurement, the solid powder was dissolved in a 1 M sulfuric acid + 0.5 M ascorbic acid solution, stirring overnight at RT.

Powder X-ray Diffraction (XRD) was carried out with a Bruker AXS-D8 Advance diffractometer (Germany) using Cu Kα (γ=1.78 Å) radiation at 35 kV and 40 mA within a 2θ range of 5 and 100° with a step size of 0.02° (2θ) and 0.15 s per step. The detector was a Bruker Lynxeye XE-T. Some analyses were performed *in situ* under air between 350 and 850 °C with a step size of 50 °C. The reactor chamber was an Anton Paar X. Previous to in situ analysis, the catalysts were preventively calcined up to 350 °C with a ramp of 1 °C min^{-1} and a dwelling time of 3 h.

The N_2 adsorption–desorption analyses were carried out on a Micromeritics Tristar 3000 instrument (USA). The sample was degassed at 170 °C overnight to remove physically adsorbed water and impurities from the surface and pores before the measurement. Specific surface area was determined by applying the BET equation in the 0.05 – 0.30 range of the adsorption isotherm. The total pore volume (V_p) was calculated from the amount of nitrogen adsorbed at a P/P_0 of 0.98 and the pore size distribution of each catalyst was drawn from the adsorption branch with the Barrett-Joyner-Halenda (BJH) method.

Diffuse reflectance UV–Vis spectra were collected using a Shimadzu UV-3600i Plus UV-Vis spectrophotometer (Japan). The powders were gently pressed in the sample holder.

X-ray Photoelectron Spectroscopy (XPS) analyses were carried out at room temperature with an SSI-X-probe (SSX 100/206) photoelectron spectrometer from Surface Science Instruments

(USA), equipped with a monochromatic Al K X-ray micro focused source (1486.6 eV). Samples were deposited onto sample holders with adhesive tape and then placed on an insulating ceramic carousel (Macor®, Switzerland). Charge effects were avoided by placing a nickel grid above the samples and using a flood gun set at 8 eV. The binding energy scale was calibrated by fixing the C-(C,H) component of the C 1s peak at 284.8 eV. Data were analysed with the CasaXPS program (Casa Software Ltd., UK). The peaks were deconvolved into a sum of Gaussian/Lorentzian (85/15) product functions after subtraction of a Shirley-type baseline.

Particle morphology was investigated through Field-Emission Scanning Electron Microscopy (FESEM) using a Zeiss Merlin microscope (Germany). Before analysis, the powder was coated with a thin layer of platinum (5 nm) via sputter deposition.

Scanning Transmission Electron Microscopy (STEM) analyses were carried out on a JEOL JEM-2100F microscope (Japan) equipped with a spherical probe aberration corrector (Cs from CEOS, Germany) and operating at 200 kV. STEM micrographs were acquired using a camera length of 12 cm and a probe size of 0.1 nm. Elemental maps were obtained by Energy Dispersive X-ray Spectroscopy (EDS) probe using a silicon drift detector (SDD) with a sensor size of 60 mm^2.

Raman spectra were acquired on a Renishaw InVia micro Raman spectrometer (UK). Three spectra were collected in different regions of each sample and averaged, using an exposure time of 225 s, a 514.5 nm excitation wavelength and a 5x objective. Prior to comparison, the spectra were normalized with respect to the intensity of ceria F_{2g} peak. The defect band was deconvoluted with three Lorentzian peaks, using Renishaw WiRE software. An additional Lorentzian peak at ca. 626 cm^{-1} was considered for the samples exhibiting the typical CuO features in their Raman spectra.

Temperature Programmed Reductions (TPR) were performed using a BELCAT II Microtrac instrument, manufactured by BEL® (Japan). A 20-40 mg catalyst sample was placed in a quartz tube, and during pre-treatment the sample was heated to 120 °C, maintained for 30 min under a 75 mL min^{-1} Ar flow. This was followed by a 30-min stabilization and cooling period in an inert atmosphere. Subsequently, a gaseous mixture of 5% H_2 in Ar at a total flow of 75 mL min^{-1} was introduced into the reactor. The temperature was then ramped from 30 °C to 900 °C at a rate of 10 °C min^{-1}, with a 20-min hold at the final temperature. Gas calibrations were performed for accurate quantification during the measurements.

2.3. Catalytic activity evaluation

CO and ethylene were taken as representative air pollutants to test the total oxidation potential of the catalysts. A fixed bed containing 50 mg of catalyst powder was prepared in a quartz U-tube reactor with an inner diameter of 4 mm. The reactor was inserted in a furnace and a thermocouple was placed approximately 1 mm above the catalytic bed. The catalyst was pretreated at 100 °C for 30 min, under a 50 mL min^{-1} flow of 10% O_2 in N_2. This flowrate corresponds to a weight hourly space velocity (WHSV) of 60000 mL h^{-1} g_{cat}^{-1} and a gas hourly space velocity (GHSV) ranging from 25000 to 80000 h^{-1}, depending on the bulk density of the catalyst.

CO oxidation tests were carried out by flowing a gas mixture consisting of 1000 ppm of CO and different amounts of O_2 (10%, 0.5% or 0.05%) in N_2, with a total 50 mL min^{-1} flowrate. The reactor temperature was increased stepwise, from RT up to a temperature in which complete CO conversion was observed (125 – 150 °C). Steps of 15 °C were performed, maintaining isothermal conditions for about 30 min for the complete stabilization of CO and CO_2 profiles before rising the temperature again (to avoid interference from possible adsorption/desorption transient phenomena). The concentration of CO and CO_2 at the reactor outlet was monitored with a continuous non-dispersive infrared analyzer (ABB Uras 14, Switzerland), while the O_2 concentration was tracked with a paramagnetic analyzer (Emerson X-stream, USA). The effect of water on the catalytic activity was also assessed, by adding 5% H_2O to the inlet flow using a Bronkhorst CEM evaporator (Netherlands). The stability of the different catalysts was evaluated by performing time on stream tests at constant temperature (90 °C) for 30 h or 100 h. Ethylene oxidation was studied in the same microreactor, by flowing a gas mixture containing 500 ppm of ethylene and 10% of O_2 in N_2, with a 50 mL min^{-1} flowrate. The reactor temperature was increased from RT with steps of 30 °C (maintained for about 30 min), until complete ethylene conversion was reached (300 – 450 °C).

3. RESULTS AND DISCUSSION

3.1. Materials structural and spectroscopic characterization: comparison between one-pot AASG synthesis vs. impregnation

The actual Cu contents measured by ICP-MS fairly matched the nominal Cu contents (Table 1). However, the experimental Cu loading was consistently slightly lower than the nominal one in all catalysts, suggesting a bias possibly due to the hygroscopic nature of the metal precursor (Cu nitrate) used in the preparation.

Table 1: Composition (ICP-MS), textural properties (N_2-physisorption), structural properties (XRD) and defects estimation (Raman spectroscopy) of the prepared catalysts.

Sample	Cu wt%[a]	SSA ($m^2\ g^{-1}$)	V_p[b] ($cm^3\ g^{-1}$)	V_{micro}[c] ($cm^3\ g^{-1}$)	D_p[d] (nm)	D_c[e] CeO_2 (nm)	D_c[e] CuO (nm)	D/F_{2g}[f]
CeO_2	/	120	0.16	0.017	6.8	7	n.m.	0.05
A-Cu5Ce	4.3	140	0.21	0.022	7.9	5	n.m.	0.95
A-Cu10Ce	8.3	130	0.16	0.027	6.8	5	n.m.	1.94
A-Cu20Ce	16.2	100	0.14	0.020	8.6	5	n.m.	1.92
I-Cu5Ce	4.7	90	0.14	0.010	6.4	7	n.m.	1.12
I-Cu10Ce	10.0	85	0.17	0.010	8.5	8	35	1.06
I-Cu20Ce	17.6	65	0.10	0.016	6.9	8	40	0.56

[a] evaluated by ICP-MS. [b] Total pore volume, estimated from the adsorption branch of the isotherm at p/p_0=0.98. [c] Microporous volume, estimated from the *t*-plot. [d] Average pore diameter, estimated from the BJH model applied on the adsorption isotherms. [e] Average crystal size evaluated by Scherrer equation, for ceria on the 28.6 ° peak (111), for CuO on the 35.6 ° peak (-111) (n.m. stands for "not measurable"). [f] Ratio between the areas of D and F_{2g} bands in Raman spectra.

Concerning the specific surface area (SSA in Table 1), the AASG procedure allows obtaining pristine ceria exposing 120 $m^2\ g^{-1}$ of surface. This value further increases (140 $m^2.g^{-1}$) when a moderate amount of Cu is added to the precursor solution to prepare one-pot samples, but slightly decreases (100 $m^2\ g^{-1}$) when the loading reaches 20 wt%. This is probably due to the concomitant increase in the micropore contribution, with respect to the pristine ceria, as shown in Table 1. The incorporation of a moderate amount of copper during the evaporation-induced self-assembly (EISA) process could cause progressive distortion of the ceria lattice. As a consequence, this distortion may lead to the formation of defective and smaller crystallites compared to pure ceria, resulting in an increased specific surface area (SSA). In fact, the defects can inhibit the migration of ceria grain boundaries and slow down the coalescence process during calcination. Conversely, Cu addition through impregnation resulted in a progressively lower SSA (as compared to the pristine ceria), caused by pore clogging since the average pore size diameter is barely affected.

All catalysts presented type IV isotherms, indicating the mesoporous nature of these materials [39], with type H2 hysteresis loops, corresponding to a complex pore structure with strong network effects (Figure 1). For catalysts prepared by one-pot AASG (Fig. 1A), the steep desorption event at p/p_0 ~0.45 is a characteristic feature that can be attributed to the tensile strength effect, which indicates the presence of mesopores smaller than ~3.8 nm [40], as confirmed by the pore size distribution graphs (Fig. 1C). The Barrett-Joyner-Halenda (BJH)

model applied on the adsorption branch of the isotherms (Fig. 1C) revealed the presence of mesopores in the 6–12 nm range (average between 7-9 nm as reported in Table 1) corresponding to the intercrystallite voids. [41] The nitrogen uptake at low relative pressure also indicates a small contribution of micropores, as confirmed by textural values reported in Table 1.

Looking at the impregnated catalysts (I-samples in Fig. 1B), isotherms retain the type IV with a H2 type hysteresis. When the Cu loading increases, the hysteresis loops progressively shift to the left and BJH pore size distribution is centered at lower diameters. This indicates progressive filling of the pores. Looking at Fig. 1D, the broad distribution of pore diameters is again attributable to intercrystallite voids rather than proper internal porosity (vide infra for TEM confirmation of catalysts morphology).

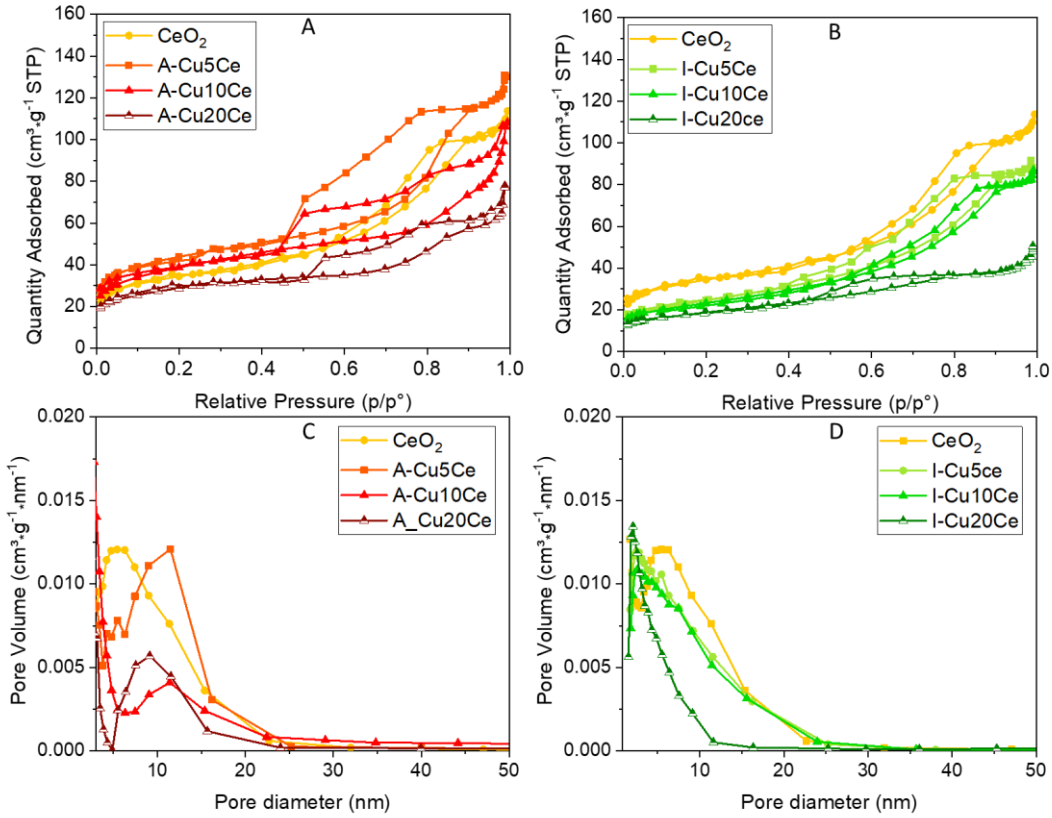

Figure 1: N_2 physisorption isotherms and pore size distribution for the one-pot catalysts (A, C) and the impregnated catalysts (B, D). Pores distribution curves were obtained via the BJH model applied on the adsorption isotherms.

The structure of the catalysts was studied by X-ray diffraction (Fig. 2). The CeO_2 pattern is characterized by broad diffraction lines that are representative of the cubic fluorite-type phase of ceria (PDF-ICDD 34-0394). The small domain of the crystallites was further confirmed by applying the Scherrer equation, revealing an average crystallite size of 7 nm. This further confirms that porosity is mainly formed by the voids between aggregated crystallites. Upon

addition of Cu by the one-pot aerosol method, no new peak is observed except for the highest copper loading, i.e. 20 wt%, where CuO diffraction signals can be detected. These signals are too low, however, to be used to evaluate the crystallite size. This reveals the high dispersion of the copper phase in all the CuO-CeO_2 catalysts prepared by one-pot aerosol (further denoted "A-catalysts"). In parallel, ceria diffraction peaks appeared wider for CuO-CeO_2 composites, signaling a ceria crystallite size slightly lower than that found for pristine CeO_2. The crystal growth was likely hindered by the presence of Cu ions in the precursor solution, and this effect probably accounts for the higher specific surface area of A-catalysts. Interestingly, CeO_2 reflection corresponding to the (222) plane of the ceria cubic structure, at $2\theta = 59.8°$, progressively disappeared when Cu loading was increased (Fig. S1). Possibly, the strong peak broadening of the reflection at 56.3 ° might have included the weak (222) reflection. However, this disappearance (probably due to the enlargement of the peak) can also be associated with the rearrangement of the ceria structure to host increasing quantities of copper into the fluorite lattice. Thus, also according to literature, the formation of Cu-O-Ce solid solution or, at highest Cu loading, mixed oxides $Cu_yCe_{1-y}O_{2-x}$, phases cannot be excluded. [42–44]

In the patterns of the impregnated catalysts (Fig. 2B), the signals of the CeO_2 phase are expectedly unaffected in the whole series, as compared to the pristine CeO_2. The typical diffraction peaks of CuO tenorite mS8 phase (PDF-ICDD 45-0937) appeared readily from I-Cu10Ce, with reflections at $2\theta = 35.6°$ and 38.8°, and became more intense for I-Cu20Ce. The estimated CuO crystal size was 35 nm for I-Cu10Ce and 40 nm for I-Cu20Ce, according to the Scherrer equation.

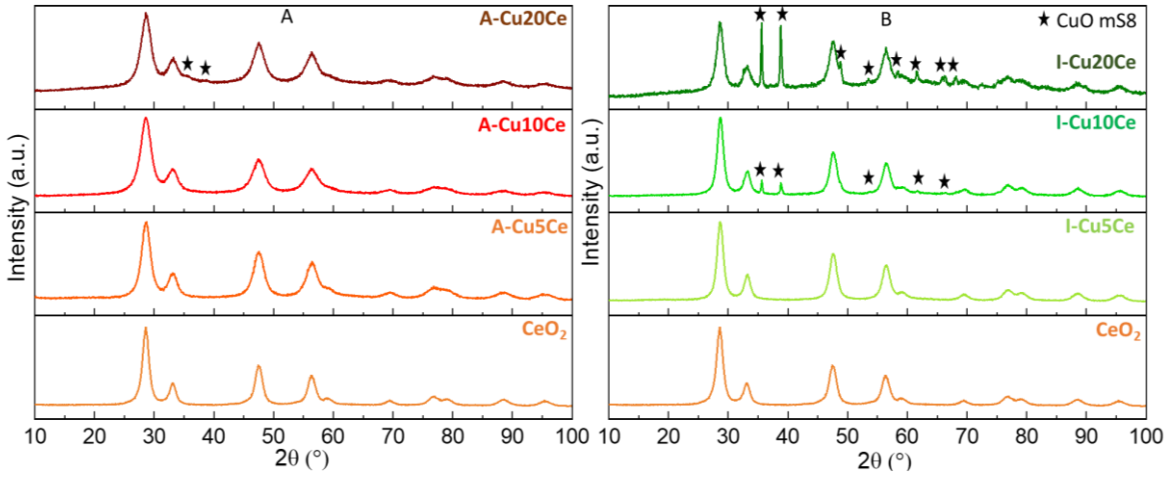

Figure 2: XRD patterns of one-pot (A) and impregnated (B) calcined catalysts.

It is well known that Cu species, even if embedded in another solid, easily tend to diffuse and sinter when temperature is raised [45]. In situ XRD was carried out over A-Cu10Ce and I-Cu10Ce

to compare the fate of CuO phase during thermal treatment (Fig. 3). Prior to in situ measurements, the A-catalyst recovered on the filters after the AASG synthesis was subjected to a preliminary calcination in static air at 350 °C to remove the surfactant. The same treatment was applied to the I-catalyst after the impregnation step. After such treatment, the impregnated catalyst already showed the diffraction signals of the CuO phase, which further increased in intensity when rising the temperature. Conversely, for A-Cu10Ce the CuO diffraction lines were only detected from 650 °C. Interestingly, they remained relatively small even when increasing the temperature up to 850 °C. All in all, the more intimate interaction created between cerium and copper oxide species by using the one-step aerosol preparation clearly led to a greater resistance to sintering, as compared to the situation obtained by using the classical impregnation technique.

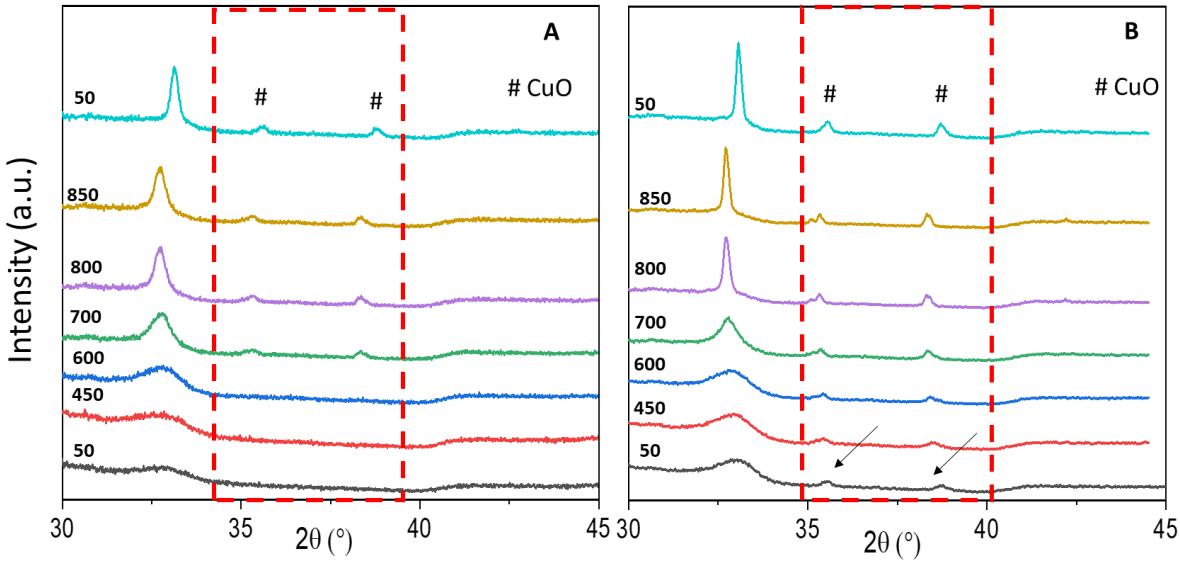

Figure 3: In situ XRD patterns collected at different temperatures for A-Cu10Ce (A) and I-Cu10Ce (B). Red frames and arrows highlight the CuO peaks emerging upon temperature increase.

Further knowledge about the structural properties of the synthesized materials was gained via Raman spectroscopy. The Raman spectra of all the AASG-made ceria-based catalysts (Fig. 4) are characterized by some common features. [46,47] The main F_{2g} peak located at about 460 cm^{-1} can be ascribed to the symmetric stretching of Ce-O bonds in the fluorite structure. The D band around 600 cm^{-1} is instead linked to the presence of different types of defects in the ceria structure, including Frenkel pairs, oxygen vacancies, and substitutional sites [48]. Finally, the large band in the 1160-1170 cm^{-1} range is related to a second-order longitudinal optical mode

(2LO). A small peak at about 825-830 cm^{-1} was also detected in the spectra of CeO_2, A-Cu5Ce and I-Cu5Ce, signaling the presence of peroxides species (O_2^{2-}) resulting from the adsorption of molecular O_2 at a surface oxygen vacancy. [49]

For the one-pot made catalysts (Fig. 4A), the position of the F_{2g} band moved from 462 cm^{-1} for the pristine CeO_2 towards lower Raman shift upon Cu addition (457 cm^{-1}), suggesting an increased distortion of the ceria structure. [47] Such shift is not observed for the catalysts made by impregnation. Regarding the defect band, pure CeO_2 is characterized by a low-intensity single component at 595 cm^{-1}, assigned to anionic Frenkel pairs. [50] Instead, Cu-doped materials exhibited a much more intense D band, including new signals at 550-555 cm^{-1} and 625-630 cm^{-1}, which can be ascribed to oxygen vacancies and oxidized substitutional sites, respectively. [48] Typical Raman features attributable to segregated CuO domains also appeared at 297, 345 and 627 cm^{-1} in the spectra of I-Cu10Ce and I-Cu20Ce [51].

The defect abundance in the various materials was compared by calculating the D/F_{2g} area ratio between the defect band and the main peak of ceria (see Table 1). A-Catalysts contain much more structural defects with respect to CeO_2, confirming that Cu ions are at least partly inserted in ceria lattice. Defectiveness strongly increased when adding up to 10 wt% of Cu, but then it remained almost constant, suggesting that Cu incorporation has reached saturation. The impregnated samples were generally characterized by a lower D/F_{2g} value, which decreased with increasing Cu loading. This is consistent with the presence of separated phases in Cu-impregnated ceria, in line with XRD results and with the presence of CuO Raman signals in the spectra of I-Cu10Ce and I-Cu20Ce[51]. The two Cu-ceria benchmark catalysts (Cu10Ce-vortex and I-Cu10Ce-comm, vide infra paragraph 3.2) exhibited CuO peaks and an even lower D/F_{2g} ratio (Fig. S2), suggesting a lower incorporation of copper in the ceria lattice.

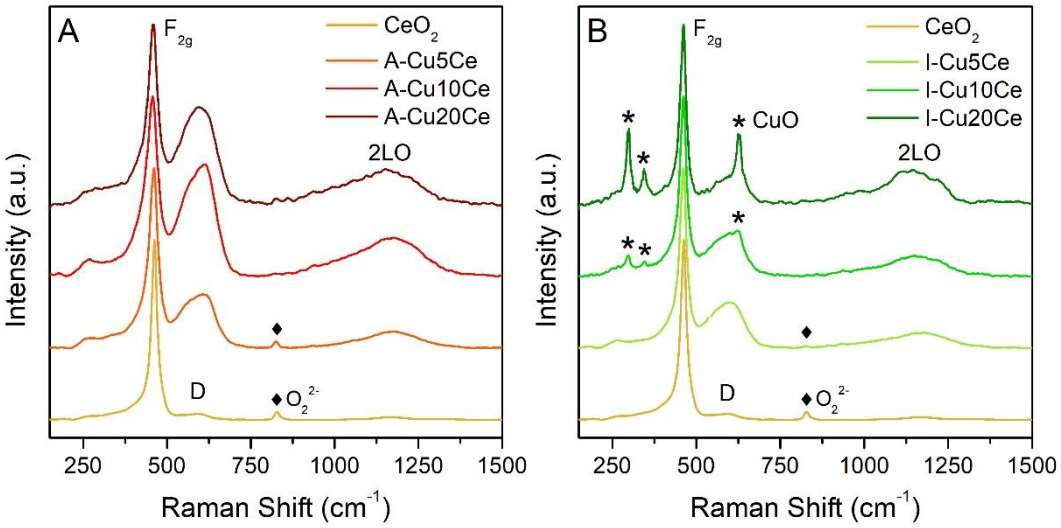

Figure 4: Normalized Raman spectra of one-pot (A) and impregnated (B) calcined catalysts.

Information on the metal coordination and environment can be obtained from the UV-Vis spectra (Fig. 5). Two bands can be seen for CeO_2-based samples: the signal at about 277 nm corresponds to the $O^{2-} \rightarrow Ce^{4+}$ charge transfer band, and the signal at 329 nm is attributed to ceria inter-band transitions. [52,53] In addition, for Cu-loaded materials, the band around 260 nm is due to $O^{2-} \rightarrow Cu^{2+}$ charge transfer transition. Additionally, in the 400 – 800 nm range, d-d orbitals electronic transitions due to Cu^{2+} ions can also be observed. This absorption can be correlated to isolated Cu based clusters. This feature is much less pronounced in the catalysts prepared by one-pot aerosol method (Fig. 5A) with respect to the impregnated catalysts (Fig. 5B). This can be ascribed to a very limited amount of bulk CuO clusters in the former samples, further suggesting that Cu^{2+} ions are intimately mixed with the ceria matrix. Accordingly, when increasing the Cu loading, a slight shift of the absorption edge to higher wavelength was observed, for A-Cu20Ce. This may be due to the incorporation of Cu cations into CeO_2 framework to form $Cu_yCe_{1-x}O_{2-x}$-type structures, that consequently led to some structural strain in the ceria lattice. [44,54] This agrees with the significant red-shift of the F_{2g} peak observed in Raman spectra. Instead, considering the Cu-impregnated catalysts (Fig. 5B), absorption in the visible range evidently increases with the copper loading. This is due to the progressively higher contribution of the d-d transition bands for Cu^{2+} in an octahedral environment. [55] These bands are mainly attributable to well distinguishable CuO species, in good agreement with XRD patterns, Raman spectra and TEM analysis (vide infra). Interestingly, in the UV-Vis spectra of I-Cu10Ce and I-Cu20Ce, an absorption shoulder arises in the range 412-475 nm, that could be attributed to small Cu_2O clusters. [56] It has been reported that the reduction of Ce^{4+} to Ce^{3+} compels copper ions to adopt a different oxidation state to maintain the lattice's charge balance. [57,58] Consequently, the substitution of Ce^{4+} with Cu^{+} can occur at the interfacial region between

copper oxide and ceria grains, owing to their similar ionic radii. This is particularly evident when well-defined CuO-CeO_2 clusters are formed, as observed in the I-catalysts. Furthermore, despite the increase in the Cu content, only a moderate red shift was observed in the absorption edge. This effect can be due to a limited but progressive increase in the size of the copper oxide nanoparticles.

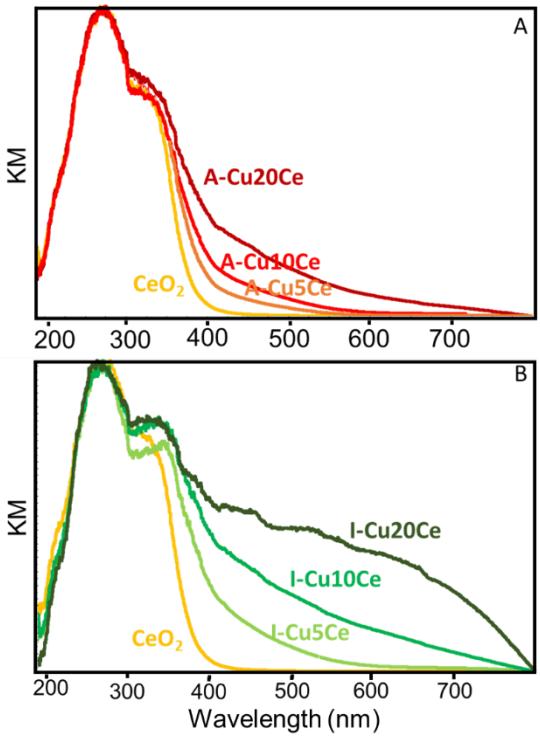

Figure 5: Diffuse reflectance UV-Vis spectra of the one-pot (A) and impregnated (B) catalysts.

To investigate the catalyst morphology, an extensive FESEM and TEM survey was carried out. Pristine CeO_2 is made of 50 nm-1 µm sized spheres (Fig. S3 and S4). This morphology is related to the spray drying process: each microsphere arises from the processing of an individual aerosol droplet. Looking at the HR-TEM images (Fig. S4), ceria crystallites with a diameter of 5-7 nm can be distinguished. Also, pores are clearly detected as brighter spots around 5 nm in size. The observed dark edges are an optical phenomenon resulting from the observation of a cross-section of a hollow sphere via TEM microscopy. At the same time, some openings or cracks seem to be visible (Fig. S4 B), suggesting the presence of hollow cavities.

Fig. 6 compares the one-pot aerosol and the impregnated catalysts. A-Cu10Ce maintained a spherical morphology with thicker edges (Fig. 6 A-F), suggesting the conservation of a hollow structure. This is confirmed by Fig. 6D which clearly shows a cavity, and similar structures were also observed elsewhere in the sample. The HR-TEM image in Fig. 6C points out Cu-

based small nanoparticles homogeneously dispersed in the ceria matrix. Finally, EDS mapping (Fig. 6E and 6F) revealed a homogeneous distribution of copper and cerium, with higher concentrations observed in the outer layer of the spheres, indicating a hollow structure. Additionally, even at the highest Cu loading (A-Cu20Ce), all the typical features previously described are essentially maintained, as evident in Fig. S5, even if slightly bigger copper aggregates can be observed in the EDS elemental mapping.

The sample morphology was very different for the impregnated catalysts (Fig. 6 G-L and Fig. S3 D). In I-Cu10Ce, the ceria microspheres forming the pristine support are no longer present, and instead, random aggregates of 6-8 nm nanoparticles are observed. This behavior indicates that the pristine microspheres are actually formed by loosely interacting crystallites (not fused together). These aggregates are dismantled under the effect of the solvent or the mechanical friction caused by the gentle mixing with a spatula during the impregnation process. Nevertheless, high homogeneity and proximity between Cu and Ce species were confirmed by EDS mapping (Fig. 6K and 6L) and high magnification images with FFT pattern (Fig. S6 A-C). In particular, some small CuO nanoparticles with an approximate diameter of 3 nm seem to be finely distributed into/onto the slightly bigger CeO_2 nanoparticles. Over I-Cu20Ce (Fig. S6 D-I), despite maintaining high elemental distribution homogeneity and small nanoparticles, some slightly bigger copper nanoparticles were also observed (Fig. S6 F).

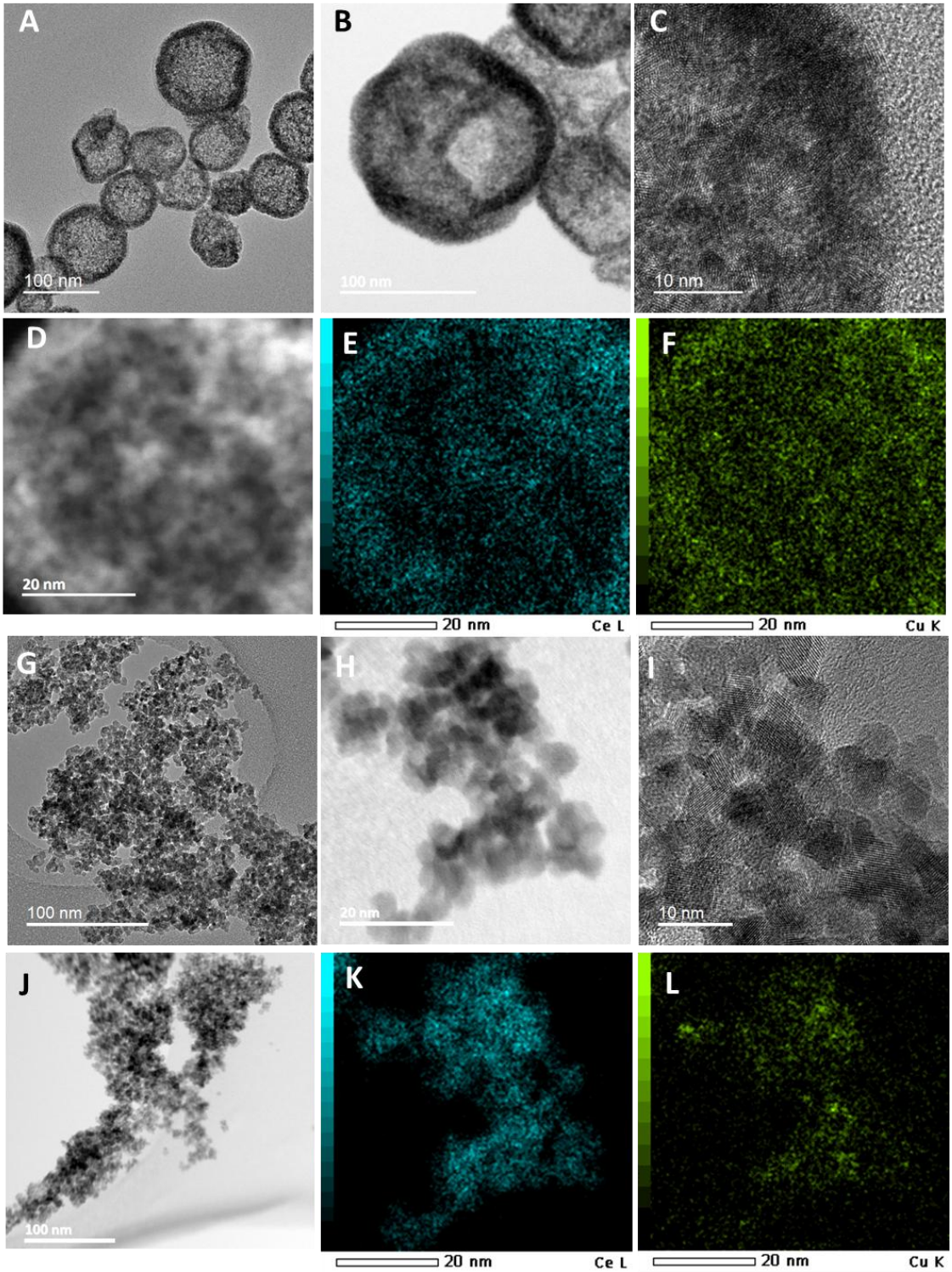

Figure 6: Typical images collected during TEM investigation of as synthesized A-Cu10Ce (A-F) and I-Cu10Ce (G-L) catalysts. Images A, B, C, D, G, H, I, J are acquired in bright field, with high magnifications at the border of a sphere (C) and of I-Cu10Ce fine nanoparticles (I). Images E, F, K, L refer to EDS elemental mapping of Ce (E, K) and Cu (F, L).

Insights into surface oxygen and cerium chemical state were obtained by XPS, as reported in Fig. S7. The O 1*s* XPS spectra presented in Fig. S7 A and B show two major contributions. The

lower binding energy peak (528.8–529.5 eV) was ascribed to the O^{2-} anions from the crystalline framework (O_β), whereas the higher binding energy peak (531.1–531.6 eV) was attributed to adsorbed surface oxygen species (O_α) such as O_2^- and O^-. [59] Ultimately, a third peak becomes discernible in the O 1*s* spectra of all the specimens, within the binding energy range of 533.6 to 534.6 eV. This peak is typically associated with weakly adsorbed species, such as OH^- and CO_3^{2-} ions. [60,61]

O_α/O_β ratios for the investigated catalysts are reported in Table S1. It is well known that ceria-based catalysts can engage in a Mars-van Krevelen mechanism, especially during oxidation of CO and VOCs. [12,62] This pathway entails the direct oxidation of pollutants using oxygen from the catalyst lattice, followed by the restoration of surface oxygen through gaseous O_2. Thus, higher O_α/O_β ratios generally indicate a higher reactivity of surface oxygen species, which can result in improved activity towards total oxidation reactions [31]. CeO_2 prepared by AASG technique exhibited a O_α/O_β value of 0.36. Also, both A-catalysts and I-catalysts always showed values between 0.30 and 0.37. The Ce 3*d* core-level spectra of the synthesized samples are shown in Fig. S7 C and D. Importantly, regardless of the preparation method, i.e. also including the commercial ceria nano-powders, the proportion of Ce^{3+} is consistently at ~20% (Table S1), revealing a defective CeO_2 surface structure.

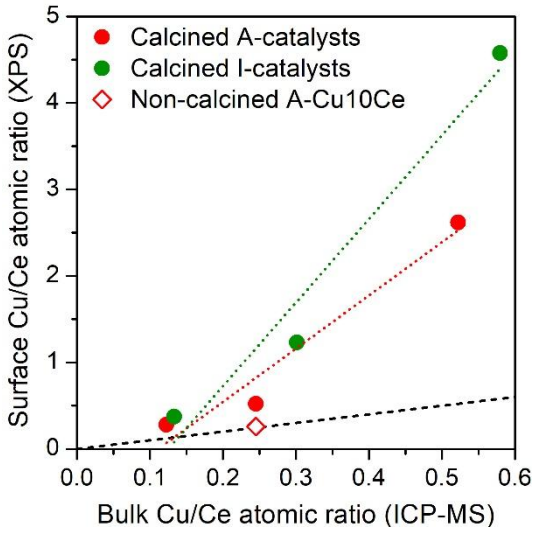

Figure 7: Correlation between surface Cu/Ce atomic ratio evaluated by XPS and the actual Cu/Ce atomic ratio measured by ICP-MS for A-catalysts (red) and I-catalysts (green). The black dashed line represents the equality line on which the surface ratio is equal to the bulk ratio. Green line and red line are only intended as a guide for the reader.

The atomic Cu/Ce surface ratio was evaluated through XPS and plotted against the bulk Cu/Ce ratio obtained by ICP analysis (Fig. 7). For both calcined A-catalysts and I-catalysts, upon increasing the Cu loading, the surface Cu concentration increased, and it was always higher than the bulk concentration, indicating that copper species are preferentially located on the catalyst surface. Logically, this is especially evident for the impregnated samples where the support is pre-formed, so the copper precursor primarily settles within the pores of ceria. Upon calcination, it predominantly migrates to the surface, leading to a higher superficial Cu/Ce ratio. In contrast, in one-pot samples, Cu is more directly and effectively integrated into the ceria structure from the very formation of the material, as the atomization of Cu and Ce precursors occurs simultaneously. As a result, a significant portion of the copper is not merely on the ceria surface, but rather incorporated within the microsphere structure.

The fact that the surface Cu/Ce ratio is markedly higher than the bulk Cu/Ce also in one-pot aerosol-made catalysts indicates that – despite forming Cu species that are well inserted in the ceria structure – Cu also tends to migrate towards the surface of the ceria nanocrystals. Calcination, as a thermal event often involving diffusion related phenomena, is often observed to provoke spatial redistribution of components of composite materials, including the migration of Cu towards the surface of another oxide. [63]

The high-resolution Cu 2p spectra are reported in Fig. S8. Consistent with literature [64], Cu $2p_{3/2}$ and Cu $2p_{1/2}$ peaks were found at ~932.8 eV and ~952.5 eV, respectively. These signals were also accompanied by two shake-up satellite peaks (~941.5 eV and ~961.6 eV), indicating the presence of CuO (Cu^{2+} with a d^9 electron configuration), in agreement with the adopted synthetic route (calcination in air). However, considering i) the small size of the satellite peak and ii) the slight shift of the peak at ~932.8 eV with respect to literature (933.5 eV), the presence of Cu_2O or Cu^0 fractions cannot be excluded. Summarizing XPS investigation, both A- and I-catalysts exhibit similar surface characteristics, showing a defective ceria structure and the presence of CuO species. All the synthesized catalysts have a high content of surface oxygen species (high O_α/O_β ratio), which can result in a higher activity towards oxidation reactions (vide infra).

TPR analyses were also carried out on the investigated catalysts (Fig. S9). Both the TPR profiles for the commercial CeO_2 nanoparticles and the aerosol-made CeO_2 are characterized by two regions of hydrogen consumption: the first one between 300 and 500 °C is attributable to the reduction of the surface of CeO_2 particles, while the second region above 700 °C is typically associated with the reduction of bulk CeO_2 to Ce_2O_3. [65,66] When copper is present in the catalyst, a complex reduction peak is observed between 100 and 300 °C. This phenomenon is attributed

to the reduction of copper oxide species and occurs at significantly lower temperatures compared to bulk CuO. [67] The first reduction component, observed near 144 °C, is associated with the smallest and finely dispersed CuO nanoparticles. [68,69] This component is predominant in I-Cu10Ce and even more pronounced in A-Cu10Ce, compared to I-Cu10Ce-comm. A second reduction peak, corresponding to the reduction of larger CuO nanoparticles, appears at 170 °C for I-Cu10Ce and A-Cu10Ce, substantially less intense than the corresponding peak observed for the commercial benchmark at 207 °C. Furthermore, the bulk ceria reduction peaks for I-Cu10Ce and A-Cu10Ce are noticeably less evident and shifted to lower temperatures (730 – 750 °C) with respect to the pristine support (790 °C). At the same time, the ceria surface reduction peak at 491 °C is almost absent in the TPR profiles of these two Cu-loaded samples. This suggests that most ceria surface and a part of bulk ceria can be reduced simultaneously with CuO at lower temperatures. The enhanced reducibility of ceria is due to the peculiar intimacy between Cu and Ce species [70]. In summary, TPR analyses indicated that the A- and I-catalysts featured smaller CuO nanoparticles with stronger interactions with the support, compared to the benchmark.

3.2 Benchmark catalysts

A-catalysts and I-catalysts will be compared with three relevant reference catalysts, which are here briefly described. A reference impregnated catalyst (I-Cu10Ce-comm) was obtained by dry impregnation of commercial cerium oxide support (nanoparticles with an average diameter 50 nm) to achieve a Cu loading of 10 wt%. It must be noted that while aerosol CeO_2 presented a O_α/O_β ratio of 0.37, this commercial ceria showed a quite lower value (0.23), indicating a lower amount of surface oxygen reactive species. Then, after impregnation with Cu and calcination, a specific surface area of 35 m^2/g was obtained. By means of XRD analysis, CuO crystallites were detected with a size of 32 nm. The presence of segregated CuO is also confirmed by clear CuO features in the Raman spectrum (see Fig. S2). In addition, this sample presents a much lower D/F_{2g} ratio compared to the I-Cu10Ce catalyst with the same Cu loading, suggesting that only a minor fraction of Cu penetrates into ceria lattice, thus generating a relatively smaller number of structural defects.

A second reference catalyst was selected among ceria-copper mixed oxides obtained through a one-pot co-synthesis, which can be compared with the AASG technique. The choice fell on one of the best samples identified in [31] (denoted as 10%$CuCeO_x$ in the original publication, and here renamed “Cu10Ce-vortex”). This material was synthesized via coprecipitation in a multi-inlet

vortex reactor and proved to have outstanding activity in total oxidation reactions when compared to other Cu/CeO_2 and even Pt/CeO_2 systems, as described in previous literature [31]. The Cu10Ce-vortex catalyst contains 10 at.% of Cu, as measured by ICP analysis. It presents intimately-mixed nanocrystals of ceria (11 nm) and CuO (7 nm), with a specific surface area of 55 $m^2\ g^{-1}$ and a D/F_{2g} ratio of 0.17 (Fig. S2).

Finally, the synthesized samples were compared with a commercial state-of-the-art oxidation catalyst (TWC), developed by a leading catalyst manufacturer. TWC is a noble metal-based material containing about 0.9 wt.% Pd + 0.1 wt.% Rh, supported on a mixed oxide made of Al_2O_3, CeO_2 and ZrO_2, used for automotive aftertreatment applications.

3.3. Catalytic performance

The catalytic properties of the synthesized materials were evaluated during CO and ethylene oxidation. In both cases, the measured O_2 consumption closely matched the CO_2 formation, confirming that complete oxidation to CO_2 was the predominant reaction pathway. Activity tests were performed by examining a series of isothermal steps, to exclude the influence of transient adsorption/desorption phenomena. The obtained conversion curves are displayed in Fig. 8, while the reaction rates and the temperatures corresponding to a 10%, 50%, and 90% conversion ($T_{10\%}$, $T_{50\%}$, and $T_{90\%}$, respectively) are reported in Table 2 and Table 3. The reproducibility of these tests can be verified by considering the example shown in Fig. S10, where the commercial TWC was tested three times, yielding almost super-imposed curves and $T_{10\%}$, $T_{50\%}$, $T_{90\%}$ values with a standard deviation smaller than 1.5 °C.

Considering ethylene oxidation (Fig. 8A and Table 2), pure CeO_2 is the least active material, showing a $T_{50\%}$ of 359 °C. A remarkable improvement can be observed upon Cu addition. All the three I-catalysts show a quite similar intermediate activity, regardless of their copper content: this corresponds to a gradual decrease of the specific reaction rate (mmol of ethylene converted per hour and per gram of copper, Table 2), moving from I-Cu5Ce to I-Cu20Ce. Instead, the performance of the A-samples progressively improves while increasing the Cu loading. Thus, A-Cu5Ce is the least active sample among the synthesized mixed catalysts; nevertheless, it is still more active than pure ceria and the two mixed Cu-Ce oxides used as references (I-Cu10Ce-comm and Cu10Ce-vortex). A-Cu10Ce is characterized by an intermediate performance, similar to that of the three I-catalysts. Finally, A-Cu20Ce exhibits the highest activity and reaction rate, with a $T_{10\%}$ as low as 200 °C. Hence, the one-pot approach allowed to preserve the intrinsic activity of copper even at high loadings, as confirmed by the nearly constant normalized reaction rate of the A-catalysts (Table 2). In general, when

comparing all the CuO-CeO_2 materials, a correlation can be found between the ethylene oxidation rate per g of Cu and the D/F_{2g} ratio reflecting the quantity of lattice defects (see Fig. S11 A). These defect sites can indeed improve the mobility of lattice oxygen and therefore promote the Mars-van Krevelen redox mechanism [71], which is often considered as the main reaction pathway for the oxidation of VOCs [72]. In fact, in this mechanism, lattice oxygen reacts with an adsorbed VOC molecule (ceria reduction), and the resulting oxygen vacancy is subsequently replenished by gaseous O_2 (ceria reoxidation) [73]. Interestingly, the performance of the A-Cu20Ce catalyst is almost on par with the one of TWC, with a $T_{50\%}$ only 13 °C higher. Although we confirm that the noble metal catalyst is very active in the oxidation of ethylene (as often reported also for other VOCs [74]), we argue that the copper-ceria materials prepared through the one-pot aerosol procedure are practical and economical alternatives.

Table 2: Catalytic performances of the catalysts during ethylene oxidation tests.

Catalyst	Specific reaction rate at 200 °C ($\mu mol_{C2H4}\ h^{-1}\ g_{cat}^{-1}$)	Normalized specific reaction rate at 200 °C ($mmol_{C2H4}\ h^{-1}\ g_{Cu}^{-1}$)	$T_{10\%}$ (°C)	$T_{50\%}$ (°C)	$T_{90\%}$ (°C)
CeO_2	53	-	248	359	461
A-Cu5Ce	54	1.25	234	298	346
A-Cu10Ce	92	1.11	211	260	296
A-Cu20Ce	226	1.39	186	226	259
I-Cu5Ce	72	1.54	213	267	314
I-Cu10Ce	103	1.03	207	256	294
I-Cu20Ce	82	0.47	209	258	301
I-Cu10Ce-comm	28	0.28	237	296	357
Cu10Ce-vortex	29	0.29	241	301	353
TWC	456	-	156	213	251

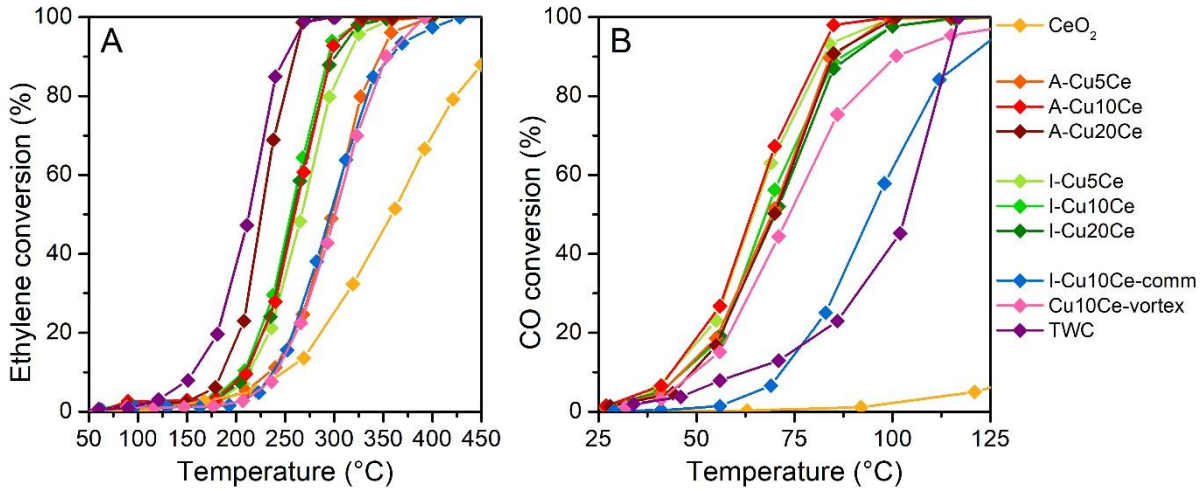

Figure 8: Evolution of the conversion as a function of the temperature during ethylene oxidation (A) and CO oxidation (B) tests performed on the synthesized samples and benchmark catalysts.

Now focusing on CO oxidation, pristine aerosol-made CeO_2 is moderately active (Fig. 8B and Fig. S12), but it is worth noting that its performance is much better than that of other pure ceria samples, obtained with different procedures but tested in analogous conditions. [71] For example, Papadopoulos et al. [75] or Zhu et al. [76] observed negligible CO oxidation at 200 °C, while here CeO_2 reaches the 50% of CO conversion at this temperature. Copper addition resulted in a marked increase in activity for both the A- and I- samples, likely due to promoted Mars-van Krevelen mechanism. All the Cu-doped catalysts showed quite similar performances regardless of synthesis method and copper loading. These materials were even able to oxidize a small fraction of the CO feed at room temperature, reaching a conversion of about 1% (10 ppm) at 25 – 27 °C. I-Cu5Ce and the three A-catalysts achieved complete CO conversion within 100 °C. Although all the conversion curves are very close, the best results were obtained with A-Cu10Ce, as highlighted by the specific reaction rate (expressed as mol of CO converted per hour and per gram of catalyst) at the onset of the light-off curve (i.e. 55 °C, see Table 3). Cu intrinsic activity (assessed by normalizing the specific reaction rate by the Cu content) decreases with the loading, especially in the case of the I-samples (see Fig. S11 B).

Table 3: Catalytic performances of the catalysts during CO oxidation tests.

Catalyst	Specific reaction rate at 55 °C ($\mu mol_{CO}\ h^{-1}\ g_{catalyst}^{-1}$)	Normalized specific reaction rate at 55 °C ($mmol_{CO}\ h^{-1}\ g_{Cu}^{-1}$)	$T_{10\%}$ (°C)	$T_{50\%}$ (°C)	$T_{90\%}$ (°C)
CeO_2	< 5	-	140	199	234
A-Cu5Ce	456	10.6	46	69	85

A-Cu10Ce	624	7.52	44	64	81
A-Cu20Ce	412	2.54	49	70	85
I-Cu5Ce	567	12.1	43	64	82
I-Cu10Ce	429	4.29	47	68	87
I-Cu20Ce	449	2.55	46	70	89
I-Cu10Ce-comm	34	0.34	72	94	120
Cu10Ce-vortex	352	3.52	50	74	101
TWC	184	-	63	102	112

Interestingly, all the catalysts prepared by AASG outperformed the three samples chosen as references. TWC, which contains Pd and Rh as active metals, was characterized by lower activity, confirming that copper-ceria catalysts can outclass commercially available and previously optimized materials based on highly active noble metals. However, when copper is loaded on commercial ceria nanoparticles instead of AASG-ceria, by using exactly the same impregnation procedure, the activity is much lower: indeed, the I-Cu10Ce-comm sample requires around 25-35 °C higher temperatures to reach the same conversion of I-Cu10Ce. This result points out that the AASG technique allows the production of a ceria support with peculiar physico-chemical properties, much more suitable for promoting copper oxidizing activity. Noticeably, the AASG-synthesized catalysts were even better than the Cu10Ce-vortex mixed oxide, that has already been shown to have outstanding performance. [31]

Further CO oxidation tests were performed to assess the catalytic activity of these mixed oxides in harsher conditions. Fig. S13 and Table S2 report the results obtained when reducing the O_2 concentration in the gas feed from 10% to 0.5% and 0.05% (the latter value representing the stoichiometric amount of O_2). This variation had minimal effects on the CO conversion curves, confirming the good ability to operate at low oxygen concentrations typical of ceria-based materials [77]. However, both the A-Cu10Ce and I-Cu10Ce samples exhibited a quite higher CO oxidation rate at intermediate O_2 concentration (0.5%). This observation suggests that competitive adsorption phenomena between CO and O_2 molecules may occur at the catalyst surface [78]. Indeed, at relatively high O_2 concentration (10%), the reaction rate could be limited by an excessive coverage of the surface by adsorbed oxygen species, resulting in less available sites for CO adsorption.

In the perspective of a real application of the AASG materials for the treatment of exhaust gases, which might contain water as a combustion product, CO oxidation was also tested in wet

conditions, with 5% of H_2O (Fig. S14). The addition of water to the reactor inlet stream resulted in a diminution of the catalytic performance (Table S3). Adverse effects of water on total oxidation catalysts are well known, both for copper-ceria systems and for noble metal-based catalysts. [79–81] These are usually ascribed to the blocking of active sites by adsorbed H_2O or to a change in the oxidation state of the metal. Here, the one-pot sample seems to be slightly more affected by humidity with respect to the impregnated one. However, despite the presence of water, both catalysts were still able to achieve complete CO conversion at 150 °C.

To investigate whether CO and ethylene oxidation influence each other, a simultaneous CO and ethylene oxidation test was performed. Previous studies have indeed reported possible interactions between CO and propylene, where the reaction pathway could shift towards either selective propylene epoxidation[82,83] or preferential CO oxidation[84], depending on the catalyst and the operating conditions. Here, for the A-Cu20Ce sample, the simultaneous oxidation test yielded conversion curves almost overlapped to those obtained when only one pollutant is fed, indicating not mutual influence (see Fig. S15).

The stability of the catalysts was assessed by performing long-term CO oxidation tests in isothermal conditions (90 °C). The aerosol-made catalysts exhibited stable activity, maintaining a steady CO conversion above 90% throughout the entire test (30 h, see Fig. 9). No significant deactivation was observed even after a 100 h CO oxidation test (see Fig. S16). Cu10Ce-vortex showed a slight decrease in CO conversion after 25 h (Fig. 9).

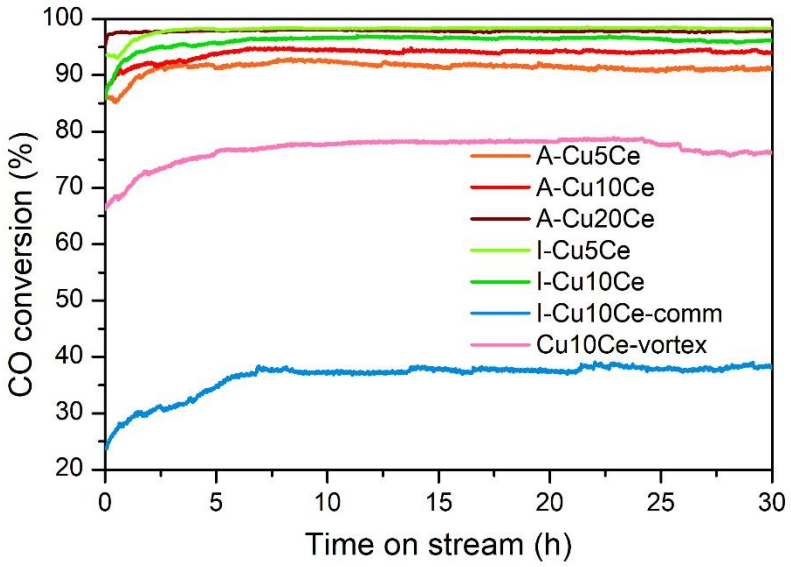

Figure 9: Evolution of CO conversion over time during long-term CO oxidation tests performed at 90 °C on the synthesized samples and benchmark catalysts.

3.4. Spent catalysts characterization

Spent catalysts were characterized to assess if they were altered by the reaction (CO oxidation up to 150 °C). Looking at the XRD pattern of the spent A-catalysts and I-catalysts (Fig. S17 A), no modifications were detected in the diffractograms of spent samples as compared to the fresh ones. The crystal size of both cerium and copper oxide also remained unaltered, revealing that no sintering phenomena occurred. Crystal size did not change even after long TOS tests at 90 °C (Fig. S17 B), underlining an optimal thermal resistance under prolonged operation.

The good structural stability of the catalysts was confirmed by collecting Raman spectra over the spent samples (Fig. S18 and S19). On A-catalysts, only minor changes in the defect band intensity were observed after short-term and long-term CO oxidation tests. Only some spent I-catalysts were characterized by a slightly lower D/F_{2g} ratio (Table S4), suggesting a lower disorder of ceria lattice. Interestingly, the peroxide peak, when visible, lost intensity after CO oxidation but did not completely disappear, suggesting that active peroxide species are continuously regenerated at the catalyst surface.

Spent materials were also studied in TEM (Fig. 10 and Fig. S20). Only over spent A-Cu20Ce (Fig. S20 I-L), a slight sintering of the small copper oxide nanoparticles can be observed, with size not exceeding 20 nm. However, all the other catalysts (both A-catalysts and I-catalysts) were not significantly affected by exposure to the reaction environment, irrespectively of the Cu loading (Fig. S20). Remarkably, the typical (deflated) spherical structure of A-Cu10Ce was maintained even after long-term tests, as revealed by Fig. 10 A and B. Elemental mapping also showed that the spheres were still homogeneous in terms of Cu and Ce distribution. Besides, also I-Cu10Ce microstructure was preserved (Fig. 10 E and F), where the dispersion of Cu throughout the CeO_2-based material seems to be maintained.

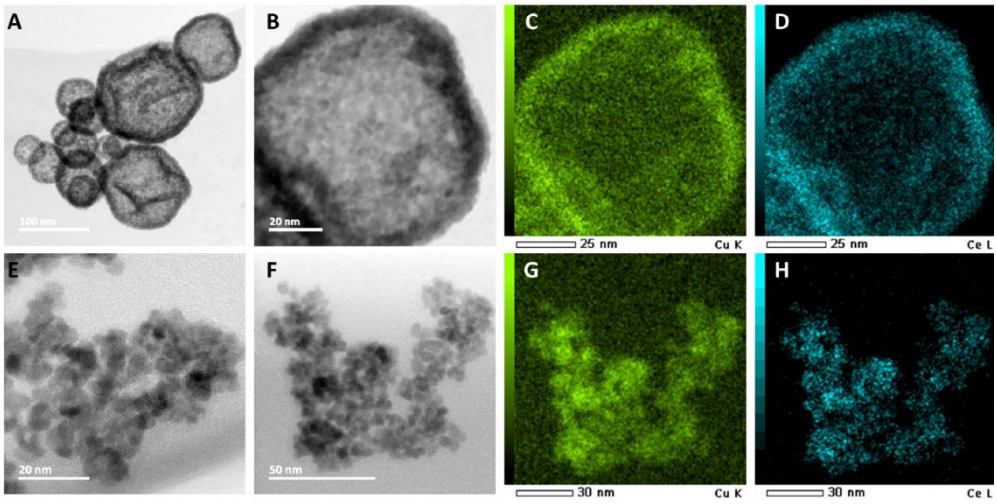

Figure 10: TEM investigation of the A-Cu10Ce (A-D) and I-Cu10Ce (E-H) spent catalysts after long-term CO oxidation stability tests. Images A, B, E, F are typical bright field images.

Images C, D refer to elemental mapping of A-Cu10Ce (B). Images G, H refer to the elemental mapping of I-Cu10Ce (F). Blue refers to Ce and green refers to Cu.

4. DISCUSSION

This section presents a detailed discussion aligning the characterization results with the catalytic activity, focusing on i) pristine AASG-made CeO_2, ii) I-catalysts, and iii) A-catalysts.

i) N_2 physisorption measurements of the CeO_2 support prepared by AASG highlighted a favorable texture for catalysis. Aerosol-made CeO_2 exhibited a SSA of 120 m^2 g^{-1} and a homogeneous distribution of mesopores centered around 7 nm. It was essentially made of 0.05 - 1 μm sized spheres constituted of finely dispersed crystallites with a diameter that was generally lower than 8 nm. Besides, XPS analysis crucially allowed correlating the O_α/O_β ratio to the oxidizing activity of ceria surface. Notably, aerosol-made CeO_2 showed a high O_α/O_β ratio of 0.36, whereas commercial ceria nano-powder displayed a ratio of 0.23. All these properties were linked to a better activity of AASG CeO_2 with respect to other commercial and literature ceria samples. For instance, despite the difficulty in comparing different experimental conditions, aerosol ceria reached T50% below 200 °C, which is a significantly lower value if compared to commercial [85], hydrothermal made [86], or precipitation made [87] ceria.

ii) SSA of impregnated I-catalysts progressively dropped upon increase of Cu loading because of pore filling, maintaining, however, values higher than 65 m^2 g^{-1} (Table 1). According to XPS, the O_α/O_β value, indicative of surface reactivity, decreased as well with increasing Cu content. Impregnated catalysts were made of random aggregates of ceria nanoparticles (7-8 nm) onto which even smaller copper oxide nanoparticles (~3-5 nm accordingly to TEM analysis) were dispersed. UV-Vis spectroscopy further confirmed that I-catalysts were mainly constituted of copper oxide nanoclusters dispersed on CeO_2 nanoparticles. Consistently, XRD and Raman features attributable to separate CuO domains were detected over I-Cu10Ce and I-Cu20Ce, which also showed a lower D/F_{2g} ratio. Thus, the addition of copper was largely compensated by its segregation, with consequent loss of Cu intrinsic activity, resulting in quite similar catalytic performances for all the three I-catalysts (Fig. 8). These samples were more active than the impregnated reference (I-Cu10Ce-comm), and also outperformed the Cu10Ce-vortex, both in CO and ethylene oxidation. In addition, they proved to be more active than commercial TWC in the case of CO oxidation. When ethylene oxidation was concerned, they had an intermediate activity, lower than that of A-Cu20Ce and TWC.

iii) The textural properties of $CuO\text{-}CeO_2$ catalysts prepared via one-pot aerosol were barely affected by the increase of Cu loading. STEM investigation showed the formation of partially hollow microspheres made of ~7 nm-sized nanocrystals, with homogeneously distributed copper species intimately mixed to cerium oxide (EDS); small Cu aggregates (~10 nm) were only observed in A-Cu20Ce. Furthermore, the XRD pattern modification, with the suppression of ceria (222) reflection upon Cu loading increase, and the absence of Cu-related reflections (very weak CuO peaks were only visible for A-Cu20Ce) suggested the formation of a mixed oxide structure. This supposition was first confirmed by in situ XRD analysis, which revealed that migration and sintering of copper oxide species upon heating treatments was drastically limited in case of the one-pot synthesis. In fact, weak and broad CuO crystalline peaks started to be barely visible only at 650 °C. UV-vis spectroscopy further supported this interpretation, showing a limited contribution of "bulk-like" CuO species. At the same time, the high degree of ceria defectiveness observed by Raman spectroscopy confirmed a progressive distortion of the ceria lattice due to copper insertion. Upon increasing the Cu loading, the surface Cu concentration (evaluated by XPS) increased quite linearly, and it was always higher than the bulk concentration (ICP), indicating that copper species were preferentially located on the catalyst surface. Such characteristic was also confirmed by TPR analysis where CuO species are readily reduced between 100 and 170 °C. These features, along with the large specific surface area, the intimate Cu-Ce interaction, the high defectiveness (D/F_{2g}, Table 1) and the presence of abundant surface reactive oxygen species (O_α/O_β, Table S1) drastically promoted the catalytic activity.

The one-pot AASG technique proved particularly advantageous for high-loading catalysts (i.e., 20 wt.% Cu). STEM analysis clearly revealed a significantly higher dispersion of Cu within the ceria spheres compared to I-Cu20Ce, where distinct CuO agglomerates were observed. The formation of bulk CuO in the latter sample, which was also confirmed by XRD and Raman analyses, resulted in reduced proximity between Cu and Ce active sites. Additionally, ceria defectiveness – an essential parameter affecting oxygen mobility which is reflected by the D/F_{2g} ratio – clearly increased with the Cu content in A-samples (i.e. $D/F_{2g} = 1.92$ for A-Cu20Ce). In contrast, I-catalysts exhibited an almost opposite trend (i.e. $D/F_{2g} = 0.56$ in A-Cu20Ce). These findings strongly emphasize that, in AASG catalysts, the simultaneous atomization of cerium and copper species allows for better Cu accommodation, ensuring much closer proximity between active sites after calcination.

Thanks to these properties, $CuO\text{-}CeO_2$ catalysts made in one-pot by ~~aerosol~~ AASG maximized the intrinsic activity of copper for ethylene oxidation even at high Cu loadings, preserving a

high normalized reaction rate (Table 2). Thus, A-Cu20Ce exhibited the best ethylene oxidation ability, outclassing both the ceria-copper reference catalysts and almost reaching the performance of the noble metal-based TWC. Regarding CO oxidation, A-Cu10Ce was the most active of all the tested samples, clearly outcompeting benchmark catalysts (Table 3).

5. CONCLUSIONS

The aerosol-assisted sol-gel method allowed synthesizing mesoporous CeO_2 made of small nanocrystals aggregated in the shape of hollow microspheres. Differently from commercial and classically prepared ceria catalysts, this material presented: high specific surface area (120 m^2 g^{-1}), small crystallites (~7 nm), relatively high concentration of structural defects, high quantity of reactive oxygen species. Furthermore, this catalyst greatly benefited from the doping with copper, which was added in two different ways. A one-pot synthesis procedure was successfully developed by directly mixing the copper and ceria precursors before spray drying, thus obtaining CuO-CeO_2 microspheres well preserving the previously described structural characteristics. Alternatively, aerosol-made ceria was impregnated with copper, forming small copper oxide nanoparticles (~3-5 nm) finely dispersed among ceria crystallites. In both cases, an extensive structural and spectroscopic characterization survey underlined a strong intimacy between copper species and CeO_2, which was especially remarkable for A-catalysts. Such favorable features, together with a high SSA and high defectivity, led to outstanding performance as compared to state-of-the-art catalysts tested under the same experimental conditions. Concerning C_2H_4 oxidation, the best aerosol-made catalyst (A-Cu20Ce) achieved a $T_{90\%}$ of 259 °C, which is comparable to the $T_{90\%}$ of 251 °C of the state-of-the-art commercial three-way catalyst (that contains Rh and Pd). In CO oxidation, the catalysts prepared by aerosol (and loaded with CuO either via impregnation or in one-pot) reached the 90% of conversion at temperatures 20-30 °C lower (80-90 °C) compared to a similar catalyst prepared with commercial CeO_2 and compared to the commercial TWC (110-120 °C). The catalysts presented here maintained their activity even at low O_2 concentration (0.05%) and revealed stable superior performances for at least 30 h (time on stream), without any apparent deactivation. This work highlights the aerosol-assisted sol-gel method as a powerful and feasible way to industrially produce high-performance copper-ceria catalysts, which could replace noble metals for total oxidation reactions.

AUTHOR CONTRIBUTIONS

The manuscript was written through contributions of all authors. All authors have given approval to the final version of the manuscript. ‡These authors contributed equally.

AKNOWLEDGMENTS

The authors kindly thank Saveria Lo Mascolo for helping in data collection and catalyst testing during the preparation of her MS thesis, and Dr. Melodj Dosa for the synthesis in the vortex reactor. D.P.D. thanks the Francqui Foundation for the Francqui Research professor chair. The authors acknowledge the project PON Ricerca e Innovazione "REACT-EU" (DM 1062/21) funded by the Italian Ministero dell'Università e della Ricerca (MUR).

APPENDIX A. SUPPORTING INFORMATION

Supplementary data associated with this article can be found in the online version at doi:

6. REFERENCES

(1) Kasab J.; Strzelec A. *Automotive Emissions Regulations and Exhaust Aftertreatment Systems.* (2020), SAE editions.

(2) Three Way Catalyst (TWC) | BASF Catalysts, https://catalysts.basf.com/products/twc-three-way-conversion-catalyst.

(3) Three-way catalyst | Umicore Automotive Catalysts, https://ac.umicore.com/en/technologies/three-way-catalyst.

(4) Karre, A. V.; Garlapalli, R. K.; Jena, A.; Tripathi, N. State of the Art Developments in Oxidation Performance and Deactivation of Diesel Oxidation Catalyst (DOC). *Catal Commun* **2023**, *179*, 106682.

(5) Busca, G. *Heterogeneous Catalytic Materials: Solid State Chemistry, Surface Chemistry and Catalytic Behaviour*; Elsevier, 2014.

(6) Li, Y.; Low, K.-B.; Sundermann, A.; Zhu, H.; Betancourt, L. E.; Kang, C.; Johnson, S.; Xie, S.; Liu, F. Understanding the Nature of Pt-Rh Synergy for Three-Way Conversion Catalysis. *Appl Catal B* **2023**, *334*, 122821.

(7) Schick, L.; Sanchis, R.; González-Alfaro, V.; Agouram, S.; López, J. M.; Torrente-Murciano, L.; García, T.; Solsona, B. Size-Activity Relationship of Iridium Particles Supported on Silica for the Total Oxidation of Volatile Organic Compounds (VOCs). *Chemical Engineering Journal* **2019**, *366*, 100–111.

(8) Wang, Z.; Zhang, L.; Ji, J.; Wu, Y.; Cai, Y.; Yao, X.; Gu, X.; Xiong, Y.; Wan, H.; Dong, L.; Chen, Y.-W. Catalytic Enhancement of Small Sizes of CeO_2 Additives on Ir/Al2O3 for Toluene Oxidation. *Appl Surf Sci* **2022**, *571*, 151200.

(9) Liu, Y.; Dai, H.; Deng, J.; Xie, S.; Yang, H.; Tan, W.; Han, W.; Jiang, Y.; Guo, G. Mesoporous Co3O4-Supported Gold Nanocatalysts: Highly Active for the Oxidation of Carbon Monoxide, Benzene, Toluene, and o-Xylene. *J Catal* **2014**, *309*, 408–418.

(10) Solsona, B. E.; Garcia, T.; Jones, C.; Taylor, S. H.; Carley, A. F.; Hutchings, G. J. Supported Gold Catalysts for the Total Oxidation of Alkanes and Carbon Monoxide. *Appl Catal A Gen* **2006**, *312* (1–2), 67–76.

(11) Chu, S.; Wang, E.; Feng, F.; Zhang, C.; Jiang, J.; Zhang, Q.; Wang, F.; Bing, L.; Wang, G.; Han, D. A Review of Noble Metal Catalysts for Catalytic Removal of VOCs. *Catalysts* **2022**, *12* (12), 1543.

(12) Wang, Q.; Yeung, K. L.; Bañares, M. A. Ceria and Its Related Materials for VOC Catalytic Combustion: A Review. *Catal Today* **2020**, *356*, 141–154.

(13) Kim, H. J.; Jang, M. G.; Shin, D.; Han, J. W. Design of Ceria Catalysts for Low-Temperature CO Oxidation. *ChemCatChem* **2020**, *12* (1), 11–26.

(14) Dong, C.; Zong, X.; Jiang, W.; Niu, L.; Liu, Z.; Qu, D.; Wang, X.; Sun, Z. Recent Advances of Ceria-Based Materials in the Oxidation of Carbon Monoxide. *Small Struct* **2021**, *2* (2).

(15) Kašpar, J.; Fornasiero, P. Nanostructured Materials for Advanced Automotive De-Pollution Catalysts. *J Solid State Chem* **2003**, *171* (1–2), 19–29.

(16) Sartoretti, E.; Novara, C.; Chiodoni, A.; Giorgis, F.; Piumetti, M.; Bensaid, S.; Russo, N.; Fino, D. Nanostructured Ceria-Based Catalysts Doped with La and Nd: How Acid-Base Sites and Redox Properties Determine the Oxidation Mechanisms. *Catal Today* **2022**, *390–391*, 117–134.

(17) Ballauri, S.; Sartoretti, E.; Novara, C.; Giorgis, F.; Piumetti, M.; Fino, D.; Russo, N.; Bensaid, S. Wide Range Temperature Stability of Palladium on Ceria-Praseodymia Catalysts for Complete Methane Oxidation. *Catal Today* **2022**, *390–391*, 185–197.

(18) Grabchenko, M. V.; Mikheeva, N. N.; Mamontov, G. V.; Salaev, M. A.; Liotta, L. F.; Vodyankina, O. V. Ag/CeO_2 Composites for Catalytic Abatement of CO, Soot and VOCs. *Catalysts 2018, Vol. 8, Page 285* **2018**, *8* (7), 285.

(19) Gaálová, J.; Topka, P. Gold and Ceria as Catalysts for VOC Abatement: A Review. *Catalysts 2021, Vol. 11, Page 789* **2021**, *11* (7), 789.

(20) Rao, K. N.; Venkataswamy, P.; Reddy, B. M. Structural Characterization and Catalytic Evaluation of Supported Copper-Ceria Catalysts for Soot Oxidation. *Ind Eng Chem Res* **2011**, *50* (21), 11960–11969.

(21) Chen, D.; Su, Z.; Si, W.; Qu, Y.; Zhao, X.; Liu, H.; Yang, Y.; Wang, Y.; Peng, Y.; Chen, J.; Li, J. Boosting CO Catalytic Oxidation Performance via Highly Dispersed Copper Atomic Clusters: Regulated Electron Interaction and Reaction Pathways. *Environ Sci Technol* **2023**, *57* (7), 2928–2938.

(22) Papadopoulos, C.; Kappis, K.; Papavasiliou, J.; Vakros, J.; Kuśmierz, M.; Gac, W.; Georgiou, Y.; Deligiannakis, Y.; Avgouropoulos, G. Copper-Promoted Ceria Catalysts for CO Oxidation Reaction. *Catal Today* **2020**, *355*, 647–653.

(23) Zheng, X.; Zhang, X.; Wang, X.; Wang, S.; Wu, S. Preparation and Characterization of CuO/CeO_2 Catalysts and Their Applications in Low-Temperature CO Oxidation. *Appl Catal A Gen* **2005**, *295* (2), 142–149.

(24) Truttmann, V.; Drexler, H.; Stöger-Pollach, M.; Kawawaki, T.; Negishi, Y.; Barrabés, N.; Rupprechter, G. CeO2 Supported Gold Nanocluster Catalysts for CO Oxidation: Surface Evolution Influenced by the Ligand Shell. *ChemCatChem* **2022**, *14* (14), e202200322.

(25) Yin, C.; Lei, Y.; Wu, H.; Xu, Y.; Luo, H.; Wang, H. Synergistic Effect of Cu and Ag on Porous (Cu, Ag) Co-Doped CeO_2 Nanosheets for Low-Temperature CO Oxidation. *Inorg Chem Commun* **2025**, *172*, 113729.

(26) Grabchenko, M. V.; Mamontov, G. V.; Zaikovskii, V. I.; La Parola, V.; Liotta, L. F.; Vodyankina, O. V. The Role of Metal–Support Interaction in Ag/CeO_2 Catalysts for CO and Soot Oxidation. *Appl Catal B* **2020**, *260*, 118148.

(27) Zhang, S.; Li, X. S.; Chen, B.; Zhu, X.; Shi, C.; Zhu, A. M. CO Oxidation Activity at Room Temperature over Au/CeO_2 Catalysts: Disclosure of Induction Period and Humidity Effect. *ACS Catal* **2014**, *4* (10), 3481–3489.

(28) Hu, J.; Wei, F.; Hu, X.; Xu, J.; Deng, W. Synthesis of CuO-Loaded Ceria Hollow Spheres for Catalytic CO Oxidation. *ChemistrySelect* **2022**, *7* (8), e202103476.

(29) Zhang, J.; Gong, M.; Cao, Y.; Wang, C. A. Facile Synthesis of Well-Dispersed CeO_2–CuO_x Composite Hollow Spheres with Superior Catalytic Activity for CO Oxidation. *RSC Adv* **2015**, *5* (115), 95133–95139.

(30) Cam, T. S.; Omarov, S. O.; Chebanenko, M. I.; Sklyarova, A. S.; Nevedomskiy, V. N.; Popkov, V. I. One Step Closer to the Low-Temperature CO Oxidation over Non-Noble CuO/CeO_2 Nanocatalyst: The Effect of CuO Loading. *J Environ Chem Eng* **2021**, *9* (4), 105373.

(31) Dosa, M.; Marin-figueredo, M. J.; Sartoretti, E.; Novara, C.; Giorgis, F.; Bensaid, S.; Fino, D.; Russo, N.; Piumetti, M. Cerium-Copper Oxides Synthesized in a Multi-Inlet Vortex Reactor as Effective Nanocatalysts for CO and Ethene Oxidation Reactions. *Catalysts* **2022**, *12* (4), 364.

(32) Wintzheimer, S.; Luthardt, L.; Cao, K. L. A.; Imaz, I.; Maspoch, D.; Ogi, T.; Bück, A.; Debecker, D. P.; Faustini, M.; Mandel, K. Multifunctional, Hybrid Materials Design via Spray-Drying: Much More than Just Drying. *Advanced Materials* **2023**, *35* (47), 2306648.

(33) Stark, W. J.; Mädler, L.; Maciejewski, M.; Pratsinis, S. E.; Baiker, A. Flame Synthesis of Nanocrystalline Ceria–Zirconia: Effect of Carrier Liquid. *Chemical Communications* **2003**, *3* (5), 588–589.

(34) Mädler, L.; Stark, W. J.; Pratsinis, S. E. Flame-Made Ceria Nanoparticles. *J Mater Res* **2002**, *17* (6), 1356–1362.

(35) Christensen, J. M.; Deiana, D.; Grunwaldt, J. D.; Jensen, A. D. Ceria Prepared by Flame Spray Pyrolysis as an Efficient Catalyst for Oxidation of Diesel Soot. *Catal Letters* **2014**, *144* (10), 1661–1666.

(36) Debecker, D. P.; Le Bras, S.; Boissière, C.; Chaumonnot, A.; Sanchez, C. Aerosol Processing: A Wind of Innovation in the Field of Advanced Heterogeneous Catalysts. *Chem Soc Rev* **2018**, *47* (11), 4112–4155.

(37) Shih, S. J.; Konstantin, B.; Liu, L. J.; Chen, C. Y. Multiporous Ceria Nanoparticles Prepared by Spray Pyrolysis. *Journal of Nanoparticle Research* **2010**, *12* (5), 1553–1559.

(38) Jia, H.; Zhu, X. M.; Jiang, R.; Wang, J. Aerosol-Sprayed Gold/Ceria Photocatalyst with Superior Plasmonic Hot Electron-Enabled Visible-Light Activity. *ACS Appl Mater Interfaces* **2017**, *9* (3), 2560–2571.

(39) Thommes, M.; Kaneko, K.; Neimark, A. V; Olivier, J. P.; Rodriguez-Reinoso, F.; Rouquerol, J.; Sing, K. S. W. IUPAC Technical Report Physisorption of Gases, with Special Reference to the Evaluation of Surface Area and Pore Size Distribution (IUPAC Technical Report). *Pure Appl. Chem* **2015**, aop.

(40) Groen, J. C.; Peffer, L. A. A.; Pérez-Ramírez, J. Pore Size Determination in Modified Micro- and Mesoporous Materials. Pitfalls and Limitations in Gas Adsorption Data Analysis. *Microporous and Mesoporous Materials* **2003**, *60* (1–3), 1–17.

(41) Sotomayor, F. J.; Cychosz, K. A.; Thommes, M. Characterization of Micro/Mesoporous Materials by Physisorption: Concepts and Case Studies. *Acc. Mater. Surf. Res* **2018**, *3* (2), 34–50.

(42) Hossain, S. T.; Azeeva, E.; Zhang, K.; Zell, E. T.; Bernard, D. T.; Balaz, S.; Wang, R. A Comparative Study of CO Oxidation over Cu-O-Ce Solid Solutions and CuO/CeO_2 Nanorods Catalysts. *Appl Surf Sci* **2018**, *455*, 132–143.

(43) Montini, T.; Melchionna, M.; Monai, M.; Fornasiero, P. Fundamentals and Catalytic Applications of CeO_2-Based Materials. *Chem Rev* **2016**, *116* (10), 5987–6041.

(44) Elias, J. S.; Artrith, N.; Bugnet, M.; Giordano, L.; Botton, G. A.; Kolpak, A. M.; Shao-Horn, Y. Elucidating the Nature of the Active Phase in Copper/Ceria Catalysts for CO Oxidation. *ACS Catal* **2016**, *6* (3), 1675–1679.

(45) Hou, X.; Zhao, Q.; Liu, Z.; Cheng, D. guo; Chen, F.; Zhan, X. Modulating Cu Species in Copper–Ceria Catalyst for Boosting CO Preferential Oxidation: Elucidating the Role of Ceria Crystal Plane. *Int J Hydrogen Energy* **2023**, *48* (64), 24697–24708.

(46) Wei, H.; Wei, T.; Li, L.; Zhang, T.; Seidi, F.; Jin, Y.; Xiao, H. Morphological Effect of Ceria-Supported Platinum Catalyst on Low-Temperature Ethylene Oxidation. *Appl Catal B* **2023**, *324*, 122242.

(47) Salomone, F.; Sartoretti, E.; Ballauri, S.; Castellino, M.; Novara, C.; Giorgis, F.; Pirone, R.; Bensaid, S. CO_2 Hydrogenation to Methanol over Zr- and Ce-Doped Indium Oxide. *Catal Today* **2023**, *423*, 114023.

(48) Sartoretti, E.; Novara, C.; Fontana, M.; Giorgis, F.; Piumetti, M.; Bensaid, S.; Russo, N.; Fino, D. New Insights on the Defect Sites Evolution during CO Oxidation over Doped Ceria Nanocatalysts Probed by in Situ Raman Spectroscopy. *Appl Catal A Gen* **2020**, *596*, 117517.

(49) Ziemba, M.; Ganduglia-Pirovano, M. V.; Hess, C. Elucidating the Oxygen Storage-Release Dynamics in Ceria Nanorods by Combined Multi-Wavelength Raman Spectroscopy and DFT. *Journal of Physical Chemistry Letters* **2020**, *11* (20), 8554–8559.

(50) Agarwal, S.; Zhu, X.; Hensen, E. J. M.; Mojet, B. L.; Lefferts, L. Surface-Dependence of Defect Chemistry of Nanostructured Ceria. *Journal of Physical Chemistry C* **2015**, *119* (22), 12423–12433.

(51) Cocuzza, C.; Sartoretti, E.; Novara, C.; Giorgis, F.; Bensaid, S.; Russo, N.; Fino, D.; Piumetti, M. Copper-Manganese Oxide Catalysts Prepared by Solution Combustion Synthesis for Total Oxidation of VOCs. *Catal Today* **2023**, *423*, 114292.

(52) Rao, K. N.; Bharali, P.; Thrimurthulu, G.; Reddy, B. M. Supported Copper–Ceria Catalysts for Low Temperature CO Oxidation. *Catal Commun* **2010**, *11* (10), 863–866.

(53) Ren, Z.; Peng, F.; Li, J.; Liang, X.; Chen, B. Morphology-Dependent Properties of Cu/CeO_2 Catalysts for the Water-Gas Shift Reaction. *Catalysts 2017, Vol. 7, Page 48* **2017**, *7* (2), 48.

(54) Elias, J. S.; Risch, M.; Giordano, L.; Mansour, A. N.; Shao-Horn, Y. Structure, Bonding, and Catalytic Activity of Monodisperse, Transition-Metal-Substituted CeO_2 Nanoparticles. *J Am Chem Soc* **2014**, *136* (49), 17193–17200.

(55) Gang, L.; Van Grondelle, J.; Anderson, B. G.; Van Santen, R. A. Selective Low Temperature NH_3 Oxidation to N_2 on Copper-Based Catalysts. *J Catal* **1999**, *186* (1), 100–109.

(56) Zabilskiy, M.; Djinović, P.; Tchernychova, E.; Tkachenko, O. P.; Kustov, L. M.; Pintar, A. Nanoshaped CuO/CeO_2 Materials: Effect of the Exposed Ceria Surfaces on Catalytic Activity in N2O Decomposition Reaction. *ACS Catal* **2015**, *5* (9), 5357–5365.

(57) Liu, W.; Flytzani-Stephanopoulos, M. Transition Metal-Promoted Oxidation Catalysis by Fluorite Oxides: A Study of CO Oxidation over Cu/CeO_2. *The Chemical Engineering Journal and the Biochemical Engineering Journal* **1996**, *64* (2), 283–294.

(58) Hočevar, S.; Krašovec, U. O.; Orel, B.; Aricó, A. S.; Kim, H. CWO of Phenol on Two Differently Prepared $CuO–CeO_2$ Catalysts. *Appl Catal B* **2000**, *28* (2), 113–125.

(59) Ballauri, S.; Sartoretti, E.; Hu, M.; D'Agostino, C.; Ge, Z.; Wu, L.; Novara, C.; Giorgis, F.; Piumetti, M.; Fino, D.; Russo, N.; Bensaid, S. Praseodymium Doping in Ceria-Supported Palladium Nanocatalysts as an Effective Strategy to Minimize the Inhibiting Effects of Water during Methane Oxidation. *Appl Catal B* **2023**, *320*, 121898.

(60) Stoch, J.; Gablankowska-Kukucz, J. The Effect of Carbonate Contaminations on the XPS O 1s Band Structure in Metal Oxides. *Surface and Interface Analysis* **1991**, *17* (3), 165–167.

(61) Frankcombe, T. J.; Liu, Y. Interpretation of Oxygen 1s X-Ray Photoelectron Spectroscopy of ZnO. *Chemistry of Materials* **2023**, *35* (14), 5468–5474.

(62) Sedmak, G.; Hočevar, S.; Levec, J. Kinetics of Selective CO Oxidation in Excess of H_2 over the Nanostructured $Cu_{0.1}Ce_{0.}9O_{2-y}$ Catalyst. *J Catal* **2003**, *213* (2), 135–150.

(63) Paris, C.; Karelovic, A.; Manrique, R.; Bras, S. Le; Devred, F.; Vykoukal, V.; Styskalik, A.; Eloy, P.; Debecker, D. P. CO_2 Hydrogenation to Methanol with Ga- and Zn-Doped Mesoporous Cu/SiO_2 Catalysts Prepared by the Aerosol-Assisted Sol-Gel Process. *ChemSusChem* **2020**, *13* (23), 6409–6417.

(64) Gong, J.; Yue, H.; Zhao, Y.; Zhao, S.; Zhao, L.; Lv, J.; Wang, S.; Ma, X. Synthesis of Ethanol via Syngas on Cu/SiO 2 Catalysts with Balanced Cu ^{0}-Cu $^{+}$ Sites. *J Am Chem Soc* **2012**, *134* (34), 13922–13925.

(65) Trovarelli, A. Catalytic Properties of Ceria and CeO_2-Containing Materials. *Catalysis Reviews* **1996**, *38* (4), 439–520.

(66) Rao, K. N.; Bharali, P.; Thrimurthulu, G.; Reddy, B. M. Supported Copper–Ceria Catalysts for Low Temperature CO Oxidation. *Catal Commun* **2010**, *11* (10), 863–866.

(67) Fedorov, A. V.; Kukushkin, R. G.; Yeletsky, P. M.; Bulavchenko, O. A.; Chesalov, Y. A.; Yakovlev, V. A. Temperature-Programmed Reduction of Model CuO, NiO and Mixed CuO–NiO Catalysts with Hydrogen. *J Alloys Compd* **2020**, *844*, 156135.

(68) Manzoli, M.; Di Monte, R.; Boccuzzi, F.; Coluccia, S.; Kašpar, J. CO Oxidation over CuO_x-CeO_2-ZrO_2 Catalysts: Transient Behaviour and Role of Copper Clusters in Contact with Ceria. *Appl Catal B* **2005**, *61* (3–4), 192–205.

(69) Si, R.; Raitano, J.; Yi, N.; Zhang, L.; Chan, S. W.; Flytzani-Stephanopoulos, M. Structure Sensitivity of the Low-Temperature Water-Gas Shift Reaction on $Cu–CeO_2$ Catalysts. *Catal Today* **2012**, *180* (1), 68–80.

(70) Konsolakis, M. The Role of Copper–Ceria Interactions in Catalysis Science: Recent Theoretical and Experimental Advances. *Appl Catal B* **2016**, *198*, 49–66.

(71) Sartoretti, E.; Novara, C.; Paganini, M. C.; Chiesa, M.; Castellino, M.; Giorgis, F.; Piumetti, M.; Bensaid, S.; Fino, D.; Russo, N. Investigation of Cu-Doped Ceria through a Combined Spectroscopic Approach: Involvement of Different Catalytic Sites in CO Oxidation. *Catal Today* **2023**, *420*, 114037.

(72) Dole, H. A. E.; Baranova, E. A. Ethylene Oxidation in an Oxygen-Deficient Environment: Why Ceria Is an Active Support? *ChemCatChem* **2016**, *8* (11), 1977–1986.

(73) Wang, Q.; Yeung, K. L.; Bañares, M. A. Ceria and Its Related Materials for VOC Catalytic Combustion: A Review. *Catal Today* **2020**, *356*, 141–154.

(74) Zhang, Z.; Jiang, Z.; Shangguan, W. Low-Temperature Catalysis for VOCs Removal in Technology and Application: A State-of-the-Art Review. *Catal Today* **2016**, *264*, 270–278.

(75) Papadopoulos, C.; Kappis, K.; Papavasiliou, J.; Vakros, J.; Kuśmierz, M.; Gac, W.; Georgiou, Y.; Deligiannakis, Y.; Avgouropoulos, G. Copper-Promoted Ceria Catalysts for CO Oxidation Reaction. *Catal Today* **2020**, *355*, 647–653.

(76) Zhu, H.; Chen, Y.; Gao, Y.; Liu, W.; Wang, Z.; Cui, C.; Liu, W.; Wang, L. Catalytic Oxidation of CO on Mesoporous Codoped Ceria Catalysts: Insights into Correlation of Physicochemical Property and Catalytic Activity. *Journal of Rare Earths* **2019**, *37* (9), 961–969.

(77) Sartoretti, E.; Fino, D.; Martini, F.; Piumetti, M.; Bensaid, S.; Russo, N. Nanostructured Equimolar Ceria-Praseodymia for Total Oxidations in Low-O_2 Conditions. *Catalysts 2020, Vol. 10, Page 165* **2020**, *10* (2), 165.

(78) Dosa, M.; Piumetti, M.; Bensaid, S.; Russo, N.; Fino, D. Novel Mn–Cu-Containing CeO_2 Nanopolyhedra for the Oxidation of CO and Diesel Soot (Part II): Effect of Oxygen Concentration on the Catalytic Activity. *Catal Letters* **2019**, *149* (1), 107–118.

(79) Ince, T.; Uysal, G.; Akin, A. N.; Yildirim, R. Selective Low-Temperature CO Oxidation over Pt-Co-Ce/Al_2O_3 in Hydrogen-Rich Streams. *Appl Catal A Gen* **2005**, *292* (1–2), 171–176.

(80) Boronin, A. I.; Slavinskaya, E. M.; Figueroba, A.; Stadnichenko, A. I.; Kardash, T. Y.; Stonkus, O. A.; Fedorova, E. A.; Muravev, V. V.; Svetlichnyi, V. A.; Bruix, A.; Neyman, K. M. CO Oxidation Activity of Pt/CeO_2 Catalysts below 0 °C: Platinum Loading Effects. *Appl Catal B* **2021**, *286*, 119931.

(81) Wang, M.; Ma, P.; Wu, Z.; Chu, S.; Zheng, Y.; Zhou, Z.; Weng, W. Evolution of Pd Chemical States and Effects of C3H6 and H2O on the CO Oxidation over Pd/CeO_2 Catalyst. *Appl Surf Sci* **2022**, *599*, 153897.

(82) Sobolev, V. I.; Koltunov, K. Y. Gas Phase Epoxidation of Propylene with CO/O_2 Mixture on Au/TiO_2. *Catal Commun* **2013**, *40*, 103–105.

(83) Sobolev, V. I.; Koltunov, K. Y. Catalytic Epoxidation of Propylene with CO/O_2 over Au/TiO_2. *Appl Catal A Gen* **2014**, *476*, 197–203.

(84) Mamontov, G. V.; Gorbunova, A. S.; Vyshegorodtseva, E. V.; Zaikovskii, V. I.; Vodyankina, O. V. Selective Oxidation of CO in the Presence of Propylene over Ag/MCM-41 Catalyst. *Catal Today* **2019**, *333*, 245–250.

(85) Akil, J.; Siffert, S.; Pirault-Roy, L.; Royer, S.; Shen, F.; Chen, W.; Cousin, R.; Poupin, C. Investigation of Catalysts M/CeO_2 (M = Pt, Rh, or Pd) for Purification of CO2 Derived from Oxycombustion in the Absence or Presence of Water. *Environmental Science and Pollution Research* **2021**, *28* (10), 12521–12532.

(86) Lykaki, M.; Pachatouridou, E.; Carabineiro, S. A. C.; Iliopoulou, E.; Andriopoulou, C.; Kallithrakas-Kontos, N.; Boghosian, S.; Konsolakis, M. Ceria Nanoparticles Shape Effects on the Structural Defects and Surface Chemistry: Implications in CO Oxidation by Cu/CeO_2 Catalysts. *Appl Catal B* **2018**, *230*, 18–28.

(87) Li, J.; Lu, G.; Wu, G.; Mao, D.; Wang, Y.; Guo, Y. Promotional Role of Ceria on Cobaltosic Oxide Catalyst for Low-Temperature CO Oxidation. *Catal Sci Technol* **2012**, *2* (9), 1865–1871.